A model study of the effects of winds on concentric rings of gravity waves from a convective plume near Fort Collins on 11 May 2004

Sharon L. Vadas,[1] Jia Yue,[2] Chiao-Yao She,[2] Peter A. Stamus,[1] and Alan Z. Liu[3]

Received 9 July 2008; revised 17 October 2008; accepted 15 December 2008; published 18 March 2009.

[1] Using a convective plume model and a ray trace model, we investigate the effects of winds on concentric rings of gravity waves (GWs) excited from a convective plume on 11 May 2004, near Fort Collins, Colorado. We find that winds can shift the apparent center of the concentric rings at z = 87 km from the plume location. We also find that critical level filtering (for GWs with small phase speeds propagating in the same direction as the wind) and wave reflection (for high-frequency GWs with small horizontal wavelengths propagating in the opposite direction to the wind) prevent many GWs from reaching the OH airglow layer. Additionally, we find that strong winds disrupt the concentric ring patterns, causing distorted "squashed" ring and arc-like patterns instead. Using a zero wind profile and a representative April mean zonal wind profile, we compare our model results with observations of concentric rings at the Yucca Ridge Field Station (40.7°N, 104.9°W). We find that the model horizontal wavelengths and periods agree reasonably well with the observed data. We also compare the model temperature perturbations with the temperature perturbations calculated from the intensity perturbations. Because the observations show less critical level filtering than from the April wind profile and more critical level filtering than from the zero wind profile, we conclude that the winds on 11 May were likely somewhat smaller than the April zonal wind profile assumed here.

Citation: Vadas, S. L., J. Yue, C.-Y. She, P. A. Stamus, and A. Z. Liu (2009), A model study of the effects of winds on concentric rings of gravity waves from a convective plume near Fort Collins on 11 May 2004, *J. Geophys. Res.*, *114*, D06103, doi:10.1029/2008JD010753.

1. Introduction

[2] When the troposphere is convectively unstable, moist air can rise quickly to the tropopause within convective plumes. If energetic enough, these plumes can push into the stably stratified stratosphere, overshooting the tropopause by up to 1–3 km [e.g., *Holton and Alexander*, 1999; *Lane et al.*, 2003]. Because the air in the stratosphere is rapidly displaced from equilibrium, it radiates gravity waves (GWs). Those GWs with large phase speeds can avoid critical level filtering from mean winds, and those GWs with small amplitudes and large horizontal and vertical wavelengths can avoid or delay wave breaking; these GWs may propagate to the mesopause, where they are often observed as straight-line perturbations in the OH airglow layer [e.g., *Swenson and Mende*, 1994; *Taylor et al.*, 1995]. Rarely, however, have they been observed as concentric rings [*Taylor and Hapgood*, 1988; *Dewan et al.*, 1998; *Sentman et al.*, 2003; *Suzuki et al.*, 2007]. Although *Taylor and Hapgood* [1988] inferred that a thunderstorm created the partial concentric rings which they observed, *Sentman et al.* [2003] showed that the concentric rings they observed originated from a severe thunderstorm.

[3] Recently, 9 nights of concentric rings were observed with the Yucca Ridge OH imager in northeastern Colorado from 2003 to 2008 [*Yue et al.*, 2009]. That paper also describes in detail the concentric rings observed on 11 May 2004; they showed that the inner and outer concentric rings are centered on two different deep convective plumes which both overshot the tropopause approximately an hour before the OH observations, and that the intervening winds between the tropopause and the OH layer were likely smaller than 20 m s^{-1}. They also showed that the behavior of the GW horizontal wavelength and period as a function of radius and time agreed reasonably well with the results from the windless Boussinesq GW dispersion relation. Here, we investigate the effects of winds on the concentric rings of GWs excited by a deep convective plume via our convective plume and ray trace models. We compare our model results with the Yucca Ridge observations on 11 May 2004 using a zero wind profile and a representative April wind model.

2. Observation of Concentric Rings in the OH Airglow Layer Near Fort Collins

[4] We utilize the images taken by the OH imager at the Yucca Ridge Field Station (40.7°N, 104.9°W) near Fort

[1]CoRA Division, NorthWest Research Associates, Boulder, Colorado, USA.
[2]Department of Physics, Colorado State University, Fort Collins, Colorado, USA.
[3]Department of Electrical and Computer Engineering, University of Illinois at Urbana-Champaign, Urbana, Illinois, USA.

Copyright 2009 by the American Geophysical Union.
0148-0227/09/2008JD010753

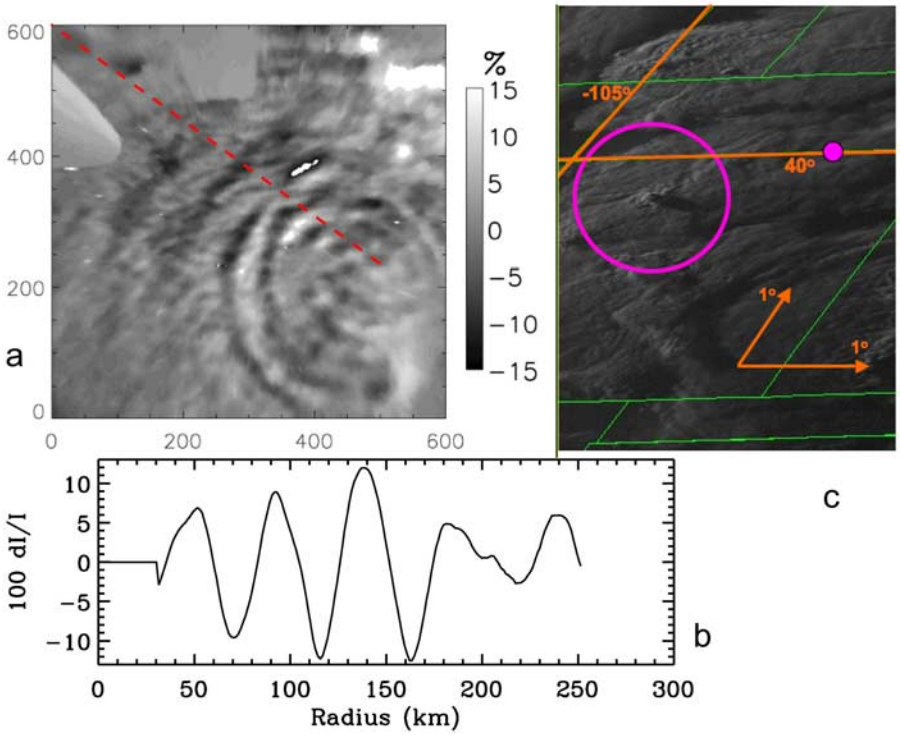

Figure 1. (a) Normalized OH airglow intensity image mapped onto the flat field at 0400 UT on 11 May 2004. The center of the concentric rings is located at 102.8°W and 40.0°N, and the x and y axes are in km. (b) Measured relative intensity perturbations $I'/\overline{I}$ (in %) at 0400 UT as a function of radius from the apparent center of the concentric rings in a direction 45° to the northwest. This direction is shown as a red dashed line in Figure 1a. (c) GOES-12 visible satellite image at 0132 UT just prior to sunset. A typical convective overshoot region during this storm period is shown in the purple circle. Green lines show the state boundaries, and orange lines show 40°N and −105°E, as labeled. The lengths of the orange arrows show 1° in the zonal and meridional directions. The purple dot shows the location of 103°W and 40°N.

Collins, Colorado, for ∼1.5 h (from 0340 to 0510 UT) on 11 May 2004 [*Yue et al.*, 2009]. We process the images as follows. First, the shutter of the imager automatically closes every hour, and records a ''dark'' image with only thermal noise. We subtract this dark image from each image. Next, we remove the stars with a median filter. Then, at each point, we calculate the deviation from the 30 min average. By doing this, we remove the continuum background brightness. Uncertainties in $I'/\overline{I}$ occur because the background brightness, $\overline{I}$, is not constant over 30 min due to city lights. Here, I' is the airglow intensity perturbations. For example, the variation of $\overline{I}$ for 0336 to 0406 UT is within ±1.5%. Therefore, we estimate the uncertainty in $I'/\overline{I}$ to be ∼1.5% during this time period.

[5] Figure 1a shows the normalized intensity of the OH airglow image at 0400 UT on 11 May 2004. The center of the OH layer is assumed to be centered at $z \sim 87$ km [*She and Lowe*, 1998]. Nearly concentric rings of GWs for ∼270° are clearly seen, with maximum intensities of ∼15%. The center of the inner rings was found to be northeast of the center of the outer rings. *Yue et al.* [2009] showed that these inner rings resulted from a convective plume (plume 1) at 103.0°W, 40.0°N, while the outer rings resulted from a convective plume (plume 2) at 103.8°W, 39.6°N. These convective plumes were separated by ∼90 km, and were strongest at 0305 UT. Figure 1b shows the measured relative intensity perturbations, $I'/\overline{I}$, as a function of radius from the apparent center of the inner concentric rings in a direction 45° to the northwest. We see that the intensity perturbations along this direction are of order ∼5–12% and are large quite close to the apparent center of the concentric rings.

3. GW Excitation From Convective Plumes

3.1. Convective Plume Model

[6] Many 3-D numerical, nonlinear and linear models of GW excitation from convection have been developed [*Lane et al.*, 2001, 2003; *Piani et al.*, 2000; *Horinouchi et al.*, 2002; *Vadas and Fritts*, 2004]. These models show that gravity waves are excited as concentric rings from vertically oriented, deep convective plumes, and propagate as concentric rings in the atmosphere if the intervening winds are small. Convective sources of gravity waves can be described analytically and equivalently as heating or momentum sources, as these sources are coupled through the vertical momentum equation. One such heating model which describes the spectrum of GWs from a deep convective source is given by *Walterscheid et al.* [2001]. The model we use here employs vertical body forces to describe the GWs excited by a deep convective plume. This model is analytic, linear, Boussinesq, neglects moisture processes, and assumes that the air above the tropopause is stationary within the frame of

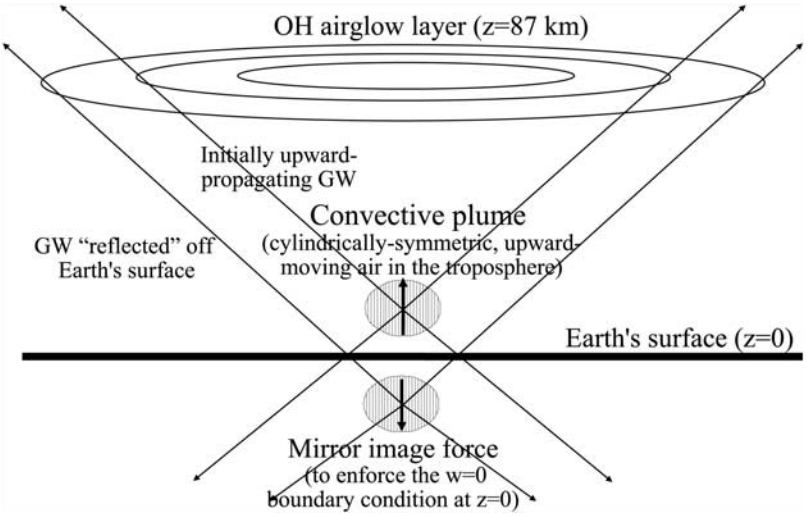

Figure 2. A sketch showing the components of the convective plume model, with an upward moving body force above the Earth's surface (labeled as convective plume) and an identical downward moving image body force "below" the Earth's surface (labeled as mirror image force). The body forces are shown as hatched ellipses, and the dark arrows in the body forces show the direction of air motion. The Earth's surface is represented by the thick horizontal black line. A few of the excited GWs are shown as thin solid lines with arrows. See text for more details.

the mean horizontal wind at the tropopause (U_{trop}), until a convective plume overshoots the tropopause and pushes the stratospheric air upward [*Vadas and Fritts*, 2009]. It solves the linear solutions in a locally unsheared environment with a constant buoyancy frequency.

[7] Observations and simulations show that there are typically many small updrafts within the "envelope" of a convectively unstable region, which give rise to a GW spectrum concentrated at small scales of ~5–10 km [e.g., *Larsen et al.*, 1982; *Alexander et al.*, 1995]. Our model neglects the individual updrafts which generate these small-scale GWs, as these GWs are not likely to propagate to the upper atmosphere and thermosphere (due to wave breaking, critical level absorption, and reflection in the stratosphere). Instead, our model calculates the spectrum of larger-scale GWs excited by the "envelope" of the upward motion of air within a convective plume. (These are the larger-scale GWs, which are more important in the mesosphere and thermosphere.) The upward acceleration of this envelope of air is modeled as a "vertical body force" in the vertical momentum equation. We also include an image (identical), but downward moving, vertical body force at an equal distance below the Earth's surface to enforce the boundary condition that the vertical velocity is zero at the Earth's surface. This also allows for the inclusion of the upward reflection of downward propagating GWs when they reach the Earth's surface.

[8] This body force (and its image) evolves in time t as $\sin^2(\pi t/\sigma_t)$ over the duration of the forcing from $t = 0$ to $t = \sigma_t$, thereby modeling a single occurrence of convective overshoot. Although GWs with periods as small as the buoyancy period are excited, the amplitudes of GWs with periods much smaller than σ_t are greatly reduced in amplitude [*Vadas and Fritts*, 2001]. For simplicity, and because we do not want our results to depend on modeled spatial features which may or may not be realistic, we represent this body force spatially as a Gaussian function in the horizontal and vertical directions, with $\mathcal{D}_H$ and $\mathcal{D}_z$ being the full width and full depth of the "envelope" of this force, respectively. Note that the typical horizontal extent of a convective plume envelope is $\mathcal{D}_H \sim$ 15–20 km. We set the top of the forcing to be at the tropopause. Therefore, the body force is maximum below the tropopause, at $z = z_{\text{trop}} - \mathcal{D}_z/2$. Simulations show that the excited GWs propagate away from the center of this body force (and from its image) [*Vadas and Fritts*, 2009]. Because GWs are actually excited from convective overshoot at or just above the tropopause in nature (since GWs cannot propagate below the tropopause in a convectively unstable atmosphere), we embed and ray trace this excited GW spectrum from the tropopause.

[9] As mentioned previously, there are many individual and localized smaller-scale updrafts within a convective plume envelope. Thus, only a fraction of the air within the envelope of a convective plume is actually entrained within upward moving air which penetrates the tropopause and excite GWs (via pushing the stratospheric air upward) at any given time. Because only a fraction of air is moving upward at the tropopause at t, and because our model neglects these smaller-scale updrafts, the amplitudes of the modeled excited GWs are larger than they should be. We take this effect into account by multiplying each excited GW's amplitude by a "filling factor" ϵ. This factor equals 1 if all of the air within the envelope is upward moving at the tropopause at t, and equals 0.5 if only 1/2 of the air within the convective plume envelope is upward moving at the tropopause at t. We estimate this fraction to be $\epsilon \sim 1/2$–$3/4$ from mesoscale simulations. This factor can be thought of as reducing the average updraft velocity of the plume envelope, by averaging over rapidly upward moving and nonmoving air parcels at the tropopause.

[10] Figure 2 shows a sketch (not to scale) of this convective plume model. The upward moving body force (labeled convective plume) and the image downward moving body

force (labeled mirror image force) both excite GWs which propagate upward and downward, as shown by the thin black lines. Because the Navier-Stokes solutions are solved for both body forces together from $z = -\infty$ to $z = +\infty$, the boundary condition that the vertical velocity, w, is zero at the Earth's surface (i.e., at $z = 0$) is automatically enforced. Although the downward moving GWs from the convective plume "pass through" the Earth's surface, the upward moving GWs (with the same horizontal and vertical wavelengths) from the image body force reach the Earth's surface at the same time; thus, a feature of this configuration is that the downward propagating GWs from the convective plume "reflect" upward at the Earth's surface. Finally, because the convective plume is cylindrically symmetric, the excited GWs follow phase surface that are in the shape of concentric rings when the winds are zero. This causes the phase surfaces to appear as concentric rings in the OH airglow layer at $z \sim 87$ km if the winds are zero (shown at the top of Figure 2).

[11] As mentioned previously, we do not take into account wind shear effects on the generated GW spectrum within the forcing area, in order to permit an analytic formulation of the solution. This is because a wind shear would cause the equations to be nonlinear [*Vadas and Fritts*, 2001]. Instead, we embed the excited GWs into the intrinsic wind frame at the tropopause (assuming a constant mean wind in the forcing area), and ray trace the GWs out of this region. Although neglecting wind shear would seem to be troublesome, it is likely an adequate assumption; *Beres* [2004] showed via comparison between linear and nonlinear models that the linear model gives reasonably good results for the excited GW spectrum with a mean background wind in the convective plume region. Also, *Lane et al.* [2003] found, using a numerical 3-D cloud-resolving model, that the excited GW spectrum in the intrinsic frame of reference is reasonably symmetric, thereby showing that the shear effect is of smaller importance than the overall Doppler effect of the moving wind frame at the tropopause.

[12] Because the upward acceleration of stratospheric air is rapid, GWs and sound waves are excited. We neglect the excitation of sound waves here, because the updraft velocity of a convective plume, $\sim$10–80 m s^{-1}, is much smaller than the sound speed, $c_s \sim 300$ m s^{-1}. The excited GWs are described by the Boussinesq dispersion relation for high-frequency GWs:

$$\omega_{Ir}^2 \simeq \frac{k_H^2 N^2}{m^2 + k_H^2}, \tag{1}$$

where ω_{Ir} is the wave's intrinsic frequency, k, l, and m are the zonal, meridional, and vertical wave numbers, respectively, $k_H^2 = k^2 + l^2$, and N is the buoyancy frequency. The zonal, meridional, and vertical wavelengths are $\lambda_x = 2\pi/k$, $\lambda_y = 2\pi/l$, and $\lambda_z = 2\pi/m$, respectively. Additionally, the horizontal wavelength is $\lambda_H = 2\pi/k_H$.

[13] Although a continuous spectrum of GWs with periods larger than the buoyancy period of $\tau_b = 2\pi/N$ are excited from a convective plume, the spectrum is maximum at a wave period determined by the plume parameters. From *Vadas and Fritts* [2001], the characteristic wave period of a cylindrically symmetric convective plume, τ_c, is determined by replacing λ_H by $\mathcal{D}_H$ and λ_z by $\mathcal{D}_z$ in equation (1). This yields the characteristic wave period:

$$\tau_c = \tau_b \sqrt{\left(\frac{\mathcal{D}_H}{\mathcal{D}_z}\right)^2 + 1}. \tag{2}$$

If the forcing is fast, i.e., $\sigma_t \ll \tau_c$, then the wave period at the maximum of the GW spectrum is $\tau_{\max} \sim \tau_c$. Otherwise, if $\sigma_t \geq \tau_c$, then the wave period at the maximum is given instead by the duration of the body force: $\tau_{\max} \sim (1-2)\sigma_t$ [*Vadas and Fritts*, 2001].

[14] Substituting $\omega_{Ir}/N = \tau_b/\tau_{\max}$ into equation (1), the ratio of the horizontal and vertical wavelengths at the peak period of the GW spectrum is

$$\frac{\lambda_H}{|\lambda_z|} \sim \sqrt{\left(\frac{\tau_{\max}}{\tau_b}\right)^2 - 1}. \tag{3}$$

This shows that the horizontal wavelengths are linearly proportional to the vertical wavelengths for GWs with periods at the peak of the convective spectrum if $\tau_{\max} \gg \tau_b$.

3.2. Ray Trace Model

[15] For each convective plume, $\sim$2 million GWs are inserted into a ray trace model appropriate for high-frequency GWs, which includes realistic temperatures, winds and thermospheric dissipation [*Vadas*, 2007]. Because thermospheric dissipation is negligible below the turbopause at $z \sim 110$ km, the anelastic GW dispersion relation for high-frequency GWs which the ray trace model solves here is

$$\omega_{Ir}^2 \simeq \frac{k_H^2 N^2}{m^2 + k_H^2 + 1/4H^2}, \tag{4}$$

where H is the density scale height [*Gossard and Hooke*, 1975]. Equation (4) differs from equation (1) in that the density scale height is assumed infinite in the Boussinesq approximation. Because of this difference, the ray trace model recalculates each GW's intrinsic frequency using equation (4) prior to ray tracing. Note that the effects of wave breaking and eddy diffusion are not included in this model. In order to investigate only the effects of varying background winds on the excited GW rings, we chose a simple isothermal profile here, with a constant temperature of $\overline{T} = 238$ K and $N = 0.02$ rad s^{-1}. The background zonal and meridional winds are $U(z)$ and $V(z)$, respectively, and vary only in altitude.

[16] GW phases were recently added to the ray trace model, thereby allowing for the reconstruction of the GW field using the GW polarization relations. Here, we assume that the waves originate from the center of the convective plume when the body force amplitude is maximum. This assumption results in velocity and temperature fields which agree well qualitatively and quantitatively with the exact Boussinesq solutions in the limit that the wave frequencies do not depend on H [*Vadas and Fritts*, 2009]. For a dissipative-

less fluid ($\nu = 0$), the GW polarization relations are [from *Vadas and Fritts*, 2005, equations (B5)–(B7)]

$$\widetilde{u_{H0}} \simeq \frac{\gamma\omega_{Ir}}{k_H \mathcal{D}}\left(m^2 + \frac{1}{4H^2}\right)\widetilde{w}_0 \tag{5}$$

$$\widetilde{T}_0 \simeq \frac{(\gamma-1)\overline{T}}{H\mathcal{D}}\left(im + \frac{1}{2H}\right)\widetilde{w}_0 \tag{6}$$

$$\widetilde{\rho}_0 \simeq -\frac{(\gamma-1)\overline{\rho}}{H\mathcal{D}}\left(im - \frac{1}{2H}\right)\widetilde{w}_0, \tag{7}$$

where $\overline{T}$ is the background temperature, $\overline{\rho}$ is the background density, $\overline{p} = R\,\overline{\rho}\,\overline{T}$ is the ideal gas law, $\overline{p}$ is the background pressure, $\gamma/(\gamma - 1) \equiv C_p/R$, C_p is heat capacity at constant pressure, and [*Vadas and Fritts*, 2005, equation (B4)]

$$\mathcal{D} = i\omega_{Ir}\left(\gamma im + \frac{1}{H} - \frac{\gamma}{2H}\right). \tag{8}$$

The quantities $\widetilde{u_{H0}}$, $\widetilde{w}_0$, $\widetilde{T}_0$, and $\widetilde{\rho}_0$ are the spectral horizontal velocity (in the direction of GW propagation), vertical velocity, temperature perturbation, and density perturbation of the GW in a scaled frame (where the GW amplitudes have been multiplied by $\exp(-z/2H)$ prior to taking the Fourier transform). Here we have assumed solutions of the form

$$\widetilde{u_H} = \widetilde{u_{H0}}\exp[i(kx + ly + mz - \omega_r t)] \tag{9}$$

for $\widetilde{u_H}$, $\widetilde{w}$, $\widetilde{\rho}$, and $\widetilde{T}$, where ω_r is the observed frequency:

$$\omega_r = \omega_{Ir} + kU + lV. \tag{10}$$

We calculate each GW's momentum flux, $\widetilde{u_{H0}}\widetilde{w}_0{}^*$, as a function of altitude during ray tracing, where * denotes the complex conjugate. These momentum fluxes and the average wave number and frequencies are binned in a 4D array in x, y, z and t, with bin sizes of 4 km, 4km, 2 km, and 2 min in the x, y, z and t directions, respectively. When all GWs have been ray traced, we calculate the spectral vertical velocity amplitude squared in each bin using equation (5) and

$$\widetilde{w}_0\widetilde{w}_0{}^* = \left(\frac{\widetilde{w}_0}{\widetilde{u_{H0}}}\right)\widetilde{u_{H0}}\widetilde{w}_0{}^*. \tag{11}$$

We then calculate the spectral horizontal velocity, temperature perturbation, and density perturbation amplitudes from equations (5), (6), and (7), respectively. The spectral zonal and meridional velocity amplitudes are then determined via

$$\widetilde{u}_0 = \frac{k}{k_H}\widetilde{u_{H0}}, \quad \widetilde{v}_0 = \frac{l}{k_H}\widetilde{u_{H0}}, \tag{12}$$

respectively. Finally, we scale all of the GW amplitudes by $\exp(z/2H)$. This yields the reconstructed GW field from ray tracing.

[17] We can gain further insight into the various dependencies of the GW amplitudes by taking the Boussinesq approximation, i.e., setting $m \gg 1/H$. In this limit, $\mathcal{D} = -\gamma\omega_{Ir}m$, and equations (5)–(7) become

$$\widetilde{u_{H0}} \simeq -\frac{m}{k_H}\widetilde{w}_0 \tag{13}$$

$$\frac{\widetilde{T}_0}{\overline{T}} \simeq -i\frac{(\gamma-1)}{H\gamma\omega_{Ir}}\widetilde{w}_0 \tag{14}$$

$$\frac{\widetilde{\rho}_0}{\overline{\rho}} \simeq i\frac{(\gamma-1)}{H\gamma\omega_{Ir}}\widetilde{w}_0. \tag{15}$$

Equations (13) and (15) agree with *Hines* [1960] for $c_s \to \infty$. Equation (13) is the familiar Boussinesq continuity equation. Using equations (14), (15), and (9), we recover the familiar Boussinesq result that the vertical velocity leads the temperature by 90° and lags the density by 90°.

[18] From equations (14) and (15), the relative temperature and density perturbations become very large as a GW approaches a critical level, since $\omega_{Ir} \to 0$ at a critical level. Because OH airglow experiments essentially measure an "integrated" GW temperature perturbation, one might suppose that OH airglow observations would "see" many GWs which are approaching their critical levels (since the temperature perturbations become extremely large there). However, because the OH layer is 8–9 km thick and because $\lambda_z \to 0$ as a GW approaches a critical level, the intensity perturbations are very small because of the cancellation effect [*Swenson and Gardner*, 1998]. We will discuss this effect, and how we use it to compare our model results with observations, in section 6.

3.3. Convective Plume Parameters

[19] As mentioned in section 2, *Yue et al.* [2009] found that two deep convective plumes at 0305 UT on 11 May 2004 near Fort Collins, Colorado, created the concentric rings in the OH airglow layer. Here, we will estimate the updraft velocity and horizontal size of these plumes for our model. We will also choose a reasonable plume depth, duration, and filling factor for these plumes.

[20] Hail was associated with the convective plumes on 11 May 2004. Sizes of 0.75–1.0 inches were reported at approximately 0300 UT according to the National Climatic Data Center Storm Event database, although larger hail was reported earlier during the storm. From *Renick and Maxwell* [1977], this "grape"-sized hail results from convective plumes with maximum updrafts of 20–30 m s^{-1}. Additionally, the Convective Available Potential Energy (CAPE) field at 0300 UT showed values of 600–900 J kg^{-1} in the vicinity of the storm. Since the maximum upward velocity in this region is

$$w \sim \sqrt{2\mathrm{CAPE}}, \tag{16}$$

this implies maximum updrafts for these plumes of $w \sim$ 35–40 m s^{-1}. Although equation (16) may be interpreted as an upper limit for the updraft velocity of a convective plume in this region, a balloon experiment during a storm showed that

the velocity of the convective updraft equaled equation (16) [*Bluestein et al.*, 1988]. We therefore choose a maximum model updraft velocity of 35 m s^{-1} here, indicative of the CAPE field and hail data.

[21] We cannot easily determine the typical horizontal sizes of the convective plumes using the NEXRAD radar data shown by *Yue et al.* [2009], because of the tilt of the radar. However, high-resolution, visible satellite images were available ~1.5 h earlier. A GOES-12 satellite image of the same region at 0132 UT is shown in Figure 1c. A convective plume which has clearly overshot the tropopause is easily seen within the purple circle, and is southwest of the locations of plumes 1 and 2 identified 1.5 h later by *Yue et al.* [2009]. Because the plumes within this storm system travelled northeastward with time, the plume shown in Figure 1c occurred within the same storm system as plumes 1 and 2, and therefore likely arose from similar convectively unstable conditions. Using this and other visible satellite images, we estimate the typical full-width horizontal sizes of plumes 1 and 2 to be ~15–20 km. For our simulations here, we choose the full-width horizontal diameter of our modeled convective plume to be $\mathcal{D}_H$ = 15 km. Additionally, the maximum possible depth of a convective plume is the depth of the troposphere plus 1–3 km. Although the tropopause is located at $z_{trop} \simeq 12$ km, we choose a somewhat smaller full depth of $\mathcal{D}_z$ = 10 km here to account for the fact that air parcels rise from the top of the mixed layer, which is typically 1–2 km above the ground. This sets the center of the body force at z = 7 km for this plume.

[22] Although *Vadas and Fritts* [2009] chose a plume duration of σ_t = 12 min, we utilize a slightly smaller plume duration here in order to better fit the OH airglow data, which contains significant intensity perturbation amplitudes near the center of the concentric GWs at small radii (see Figure 1b). The concentric rings at small radii are formed from the highest-frequency GWs in the excited spectrum. Because the excited GW amplitudes are increasingly small for wave frequencies much smaller than $2\pi/\sigma_t$ [*Vadas and Fritts*, 2001], we choose a smaller plume duration of σ_t = 10 min here in order to allow for the excitation of GWs with periods of ~5–10 min that have larger wave amplitudes than for σ_t = 12 min. This chosen duration is reasonable, because the movement of air which excites the GWs (the upwelling just below the tropopause, the overshoot, and the collapse back down to the tropopause) lasts for approximately 5–15 min in typical convective simulations.

[23] Finally, we set the filling factor for the modeled plume to be

$$\epsilon = 3/4. \tag{17}$$

[24] Figure 3 shows the GW spectrum excited by this model convective plume. The amplitudes correspond to the horizontal velocity amplitudes of the GWs at z = 87 km if the intervening winds are zero. We also overlay the intrinsic horizontal phase velocity (blue dashed lines), $c_{IH} = \omega_{Ir}/k_H$, and the vertical group velocity (pink dash-dotted lines),

$$c_{g,z} = \frac{\partial \omega_{Ir}}{\partial m}. \tag{18}$$

The peak of this spectrum occurs at $\lambda_H \sim 50$ km and $\lambda_z \sim 25$ km, although there is a smaller peak at $\lambda_H \sim 30$ km and $\lambda_z \sim 11$ km. The doubl nature of this spectrum occurs

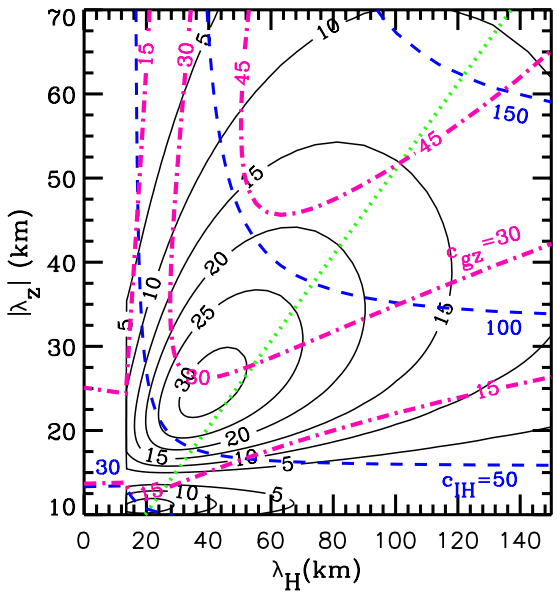

Figure 3. Excited GW spectrum from the modeled convective plume (including the body force image). Shown are the GW horizontal velocity amplitudes at z = 87 km in intervals of 5 m s^{-1} if the winds are zero (solid black lines). These are the maximum amplitudes at this altitude. Dash-dotted pink lines indicate the vertical group velocity, c_{gz}, in 15 m s^{-1} intervals, as labeled. Dashed blue lines indicate the intrinsic horizontal phase speed, c_{IH}, for 30, 50, 100, and 150 m s^{-1}, as labeled.

because of the reflection of GWs off the Earth's surface, and is seen in the intrinsic GW spectra in fully 3-D numerical models as well [e.g., *Lane et al.*, 2003, Figure 20]). Convective models which do not include the Earth's surface have only a single peak [*Vadas and Fritts*, 2004]. This spectrum also peaks at intrinsic horizontal phase speeds of $c_{IH} \sim 60$–70 m s^{-1}. Here, intrinsic denotes the motion of the GWs with respect to the reference frame of the moving air at the tropopause. (For example, if the wind at the tropopause is eastward with $U \sim 20$ m s^{-1}, then an eastward propagating GW with $c_{IH} \sim 30$ m s^{-1} has an observed phase speed of c_x = 10 m s^{-1}. But if the same GW is westward propagating, its observed phase speed is c_x = 50 m s^{-1} instead.) Note that virtually all of the GWs in our model have intrinsic phase speeds of $c_{IH} > 30$ m s^{-1}.

[25] From equation (2), the characteristic wave period of this convective plume is τ_c = 9 min, which is approximately the same as the force duration; therefore, the GW spectra peaks at $\tau_{max} \sim (1–2)\sigma_t \sim 10–20$ min. We overlay equation (3) in Figure 3 with τ_{max} = 11 min as a dotted green line. Although the GWs at and near the spectral peak have wave periods of 11 min, larger λ_H GWs with smaller wave amplitudes typically have larger wave periods (i.e., values of λ_z below the dotted line). Note that convectively generated GWs with small (large) λ_H have small (large) λ_z along the "ridge" of the spectrum.

4. Winds Used for the Model Simulations

[26] Although the zonal and meridional winds caused by tides and planetary waves vary throughout the day, there is a

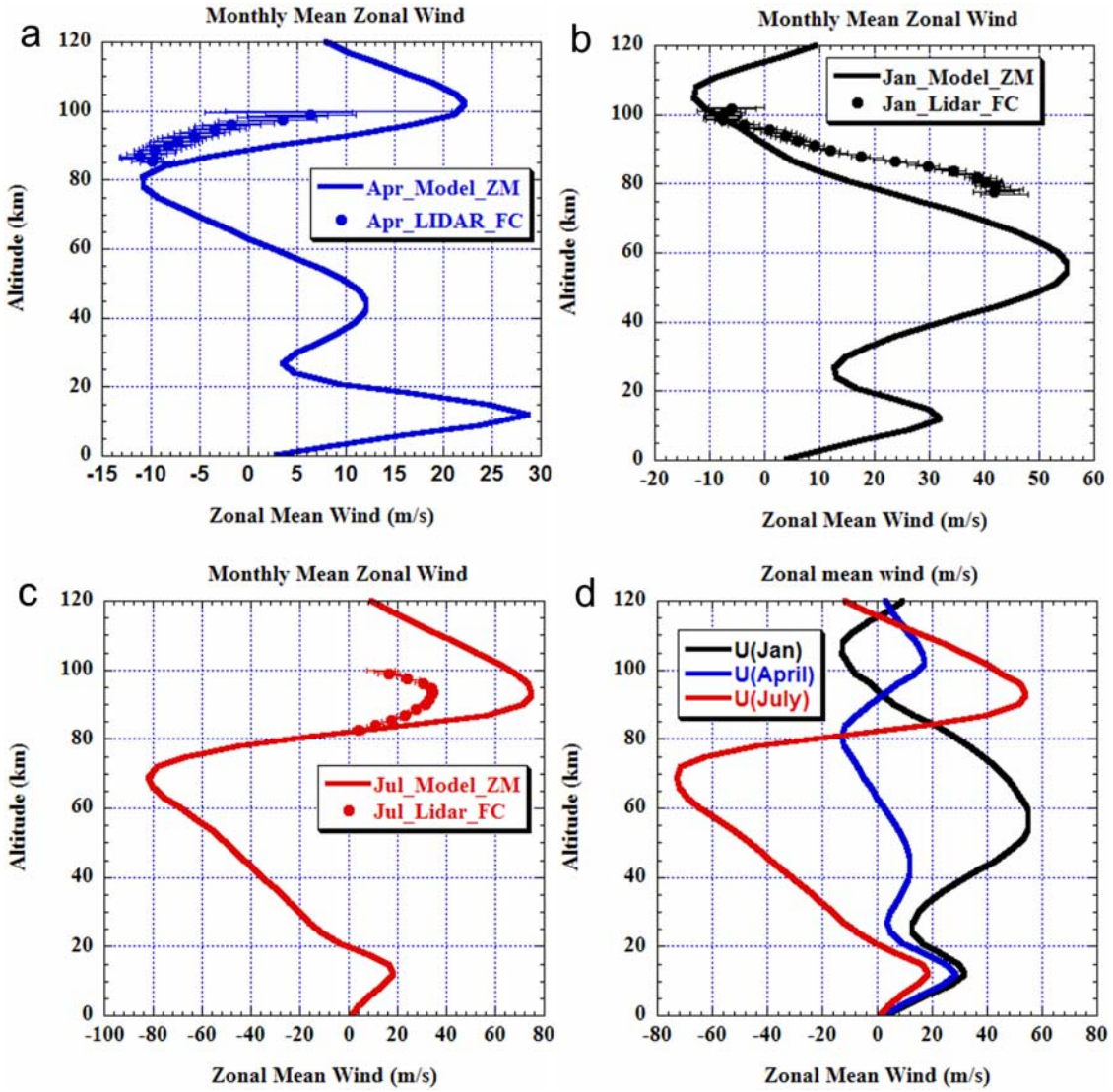

Figure 4. Representative monthly mean zonal winds at Fort Collins, CO. (a–c) Monthly mean winds for April, January, and July with blue, black, and red colors, respectively. The lines and dots (with error bars) show the values from the HAMMONIA-GCM and Na Lidar observations, respectively. (d) Representative winds for April, January, and July as blue, black, and red lines, respectively, constructed from the model and observational results of Figures 4a–4c in order to achieve a smooth transition from one region to another. (See text for explanation.)

difference in monthly means (climatology) between zonal and meridional winds. While they both exhibit seasonal variations, the magnitudes of the monthly mean zonal winds are typically much larger than those of the monthly mean meridional winds, and the monthly mean zonal winds are representative of diurnal or hourly winds. Thus, we investigate the effects of winds on concentric GWs with 3 monthly mean zonal wind profiles in January, April, and July representing winds under winter solstice, equinox and summer solstice conditions, respectively. Figures 4a, 4b, and 4c show monthly mean zonal-mean zonal winds, U, at 41°N from the HAMMONIA general circulation model [*Schmidt et al.*, 2006] for April, January, and July as blue, black, and red lines, respectively. Additionally, we overlay the corresponding Na lidar observations in the mesopause region over Fort Collins, Colorado, with dots and error bars [*Yuan et al.*, 2008]. Notice the general agreement between HAMMONIA and lidar winds in the mesopause region (80–100 km), although there is a noticeable difference in July. Using these data, we construct typical zonal wind profiles for the model simulations performed here by taking the HAMMONIA output between the ground and 60 km, and the average of the lidar and HAMMONIA data between 80 and 100 km. We also ensure smooth transitions between 60 and 80 km and between 80 and 120 km via educated guesses. This process leads to the profiles shown in Figure 4d. From Figure 4d, the typical mean winds in April (at the spring equinox) are smaller than 30 m s^{-1}, and are smaller than the mean winds in January and July. The January winds are dominated by a strong eastward wind

in the mesosphere of 50 m s^{-1}, although the wind is approximately zero in the OH airglow layer. The July winds are dominated by a strong westward wind of -70 m s^{-1} in the mesosphere and a strong eastward wind in the OH airglow layer of 50 m s^{-1}. Note that for all three seasons, the winds are moderate at the tropopause, $\sim$15–30 m s^{-1}.

[27] The April monthly zonal-mean zonal wind profile is similar to the zonal wind profile inferred from the Denver balloon sounding and the Thermosphere-Ionosphere-Mesosphere-Electrodynamics General Circulation Model (TIME-GCM) [*Roble and Ridley*, 1994] on 11 May 2004. From this, the inferred zonal wind is $U \sim 15$ m s^{-1} at the tropopause, decreases to $U \sim -20$ m s^{-1} at $z \sim 70$ km, then increases sharply to $U \sim 20$ m s^{-1} at $z \sim 87$ km [*Yue et al.*, 2009]. In contrast, the April zonal model winds in Figure 4d is larger, $U \sim 30$ m s^{-1}, at the tropopause, decreases to $U \sim -10$ m s^{-1} at $z \sim 80$ km, and increases to $U \sim -5$ m s^{-1} at $z \sim 87$ km. The main difference between these wind profiles is that below 80 km, the representative April zonal mean winds are consistently $\sim$10–15 km eastward of the balloon sounding and TIME-GCM winds, although the shapes of the profiles are very similar. Although the TIME-GCM wind shear is larger above 80 km, the GWs do not propagate very far through this shear before reaching the mesopause; therefore, it likely does not appreciably affect the concentric ring patterns in the airglow layer. Finally, we note that the meridional wind profiles inferred from the Denver balloon soundings and the TIME-GCM on 11 May 2004 above the tropopause are less than 10 m s^{-1}, and are thus very small. Therefore, we can compare the results obtained here using only the April zonal mean monthly zonal winds (with zero meridional winds) with the observed results on 11 May 2004, near Fort Collins. Note that in general, the hourly meridional winds during January and July will typically be as large as the hourly zonal winds.

5. Effects of Winds on GWs From Modeled Convective Plumes

[28] We now investigate the effects of background winds on the concentric rings of GWs excited from vertically oriented convective plumes. We use the zero winds and the zonal winds from Figure 4d. For each wind profile, we embed the GW spectrum excited from the convective plume into the wind frame moving at the speed of the horizontal wind at the tropopause, $U_{\rm trop} = U(z_{\rm trop})$, because the excited spectrum is reasonably symmetric in the intrinsic reference frame [*Lane et al.*, 2003]. We then ray trace these GWs from the convective overshoot time and location of $t = 0$ min, $x = y = 0$, and $z = z_{\rm trop} = 12$ km (the altitude of the tropopause). We show the resulting temperature perturbations at $z = 87$ km at $t = 50$, 70, 90, 120 min in Figures 5 and 6. Here, we have used the anelastic polarization relation to calculate the temperature perturbation, equation (6). In Figures 5 (left) and 5 (right), we show the GWs ray-traced through zero winds and the April zonal winds from Figure 4d, respectively. In Figures 6 (left) and 6 (right), we show the GWs ray-traced through the January and July zonal winds from Figure 4d, respectively.

[29] When the winds are zero, then symmetric, concentric rings of GWs propagate through the airglow layer. Although the concentric rings move outward in time at a fixed altitude, each wave is actually moving upward and outward, as sketched in Figure 2. A single concentric ring in the zero-wind case contains GWs having the same frequency (but propagating in different directions), since the wave's intrinsic frequency using the Boussinesq relation is

$$\omega_{Ir} \sim N \cos\theta, \tag{19}$$

where θ is the angle of the GW's raypath from the zenith (vertical). Thus, higher-frequency GWs propagate close to vertical, while lower-frequency GWs propagate more horizontally [*Hines*, 1967]. The circular concentric rings result from the cylindrical symmetry of the vertically moving updrafts. Note that updrafts which are tilted with respect to the vertical break this symmetry, and result in asymmetric GW ring patterns even when the winds are zero (S. L. Vadas, personal communication, 2009). Here, tilted plumes can be caused by strong wind shears below the tropopause.

[30] A quick glance at Figures 5 and 6 reveals that when the winds are nonzero, many of the GW rings are distorted, especially at late times, appearing as "squashed" rings and partial arcs. Additionally, there are many regions where there are no GWs at all (grey shading). There are also substantial shifts in the apparent centers of the concentric rings in the OH layer from the convective plume location (at $x = y = 0$) when the winds are strong; this is especially apparent when the GWs propagate through the January and July zonal wind profiles.

[31] Consider the GWs ray-traced through the April zonal winds. First, the center of the concentric GWs (CGWs) is very close to the location of the convective plume at $x = y = 0$; at $t = 50$ min, for example, the apparent center is at $x \simeq 10$–20 km. This shift is small because the intervening winds are small. Additionally, although the rings are mostly 360° for $t = 50$ min, the amplitudes of the highest-frequency, eastward propagating GWs (with radii $r \simeq 40$–80 km, as measured from the apparent center of the CGWs) are much larger than those of the highest-frequency, westward propagating GWs at $t = 50$ min and $r \simeq 40$–80 km. For $t \geq 70$ min, however, the amplitudes are much larger for the westward propagating GWs for $r > 150$ km. Additionally, for $t \geq 70$ min, most of the eastward propagating GWs are either missing or have relatively small amplitudes at $z = 87$ km; at these times, the spectrum is dominated by GWs propagating rearward to the direction of the wind at the tropopause, similar to *Fovell et al.* [1992].

[32] All of these results can be explained by mean wind Doppler shifting. The wind at the tropopause is $U_{\rm trop} = U(z_{\rm trop}) \sim 25$ m s^{-1}, and the wind at $z = 87$ km is zero. The intervening winds are relatively small, with average speeds of $U \sim 10$ m s^{-1}. Over 50 min, this causes an average displacement of the center of the CGW by 30 km. This explains the eastward displacement of the apparent center of the CGW with respect to the plume location. Next, the intervening winds are westward in the frame of the wind at the tropopause, $U_{\rm trop}$. GWs with the same λ_z and $|\lambda_x|$ are excited with the same amplitude moving eastward and westward and at the same angles with respect to the vertical in the frame of $U_{\rm trop}$. The angles are determined by each wave's intrinsic frequency ω_{Ir} from an anelastic formula

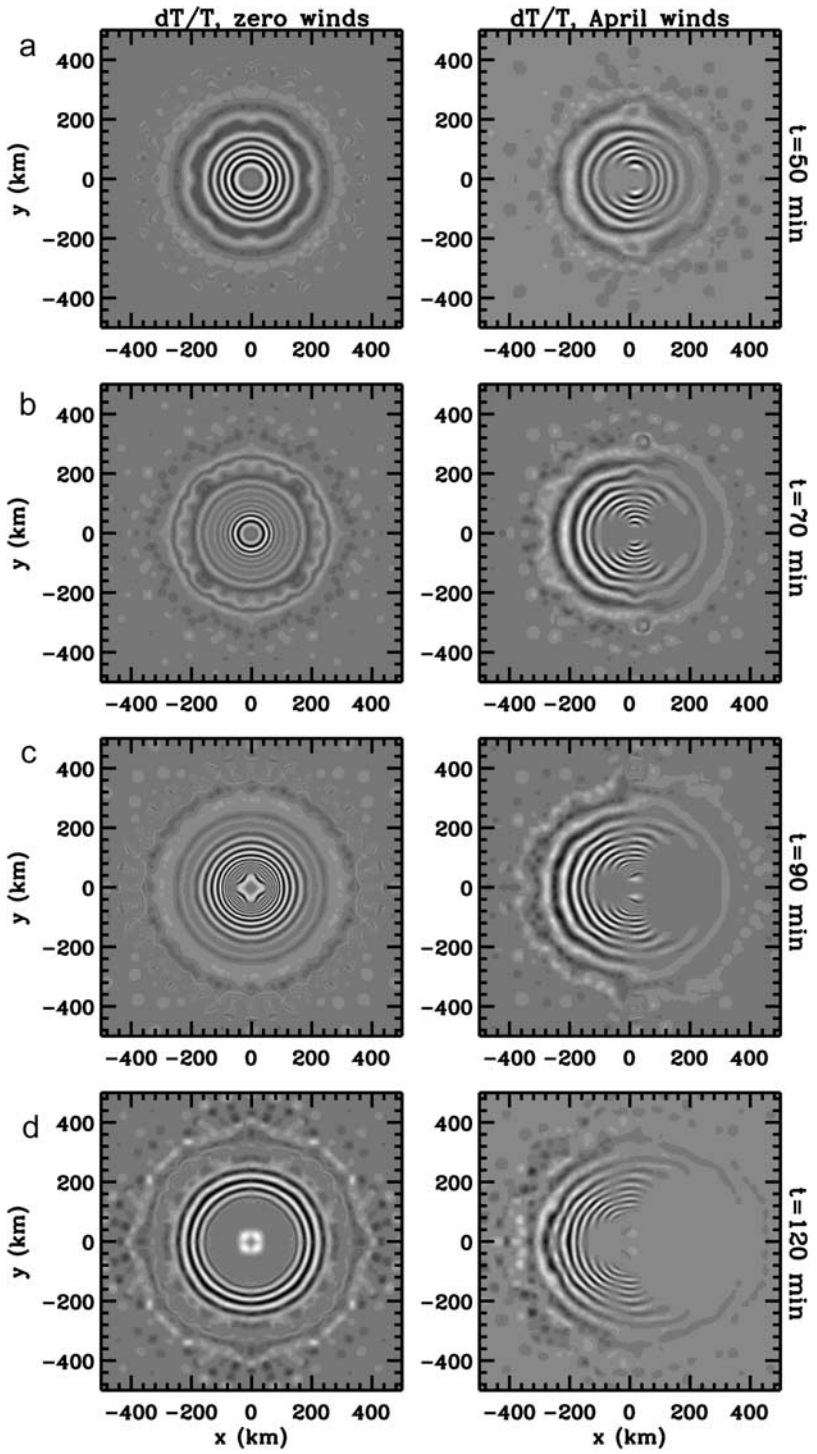

Figure 5. GW temperature perturbations at $z = 87$ km at $t = 50$, 70, 90, and 120 min from top to bottom, respectively. (left) The zero wind results and (right) the April zonal wind results are shown. Maximum positive and negative values are shown as light and dark shading, respectively. From left to right, the maximum values of $|T'/\overline{T}|$ are (a) 6.9 and 6.4%, (b) 5.3 and 4.3%, (c) 3.6 and 3.4%, and (d) 0.9 and 2.4%.

analogous to equation (19). A GW's ground-based (or observed) wave frequency is then

$$\omega_r = \omega_{Ir} + kU, \tag{20}$$

since the meridional wind is zero here, $V = 0$. Because the background winds and tem eratures are constant in time, ω_r is constant for each wave, and because the background winds and temperatures only depend on z, k is constant for each wave [*Lighthill*, 1978]. Therefore a GW's intrinsic frequency at the altitude z is

$$\omega_{Ir}(z) = \omega_{Ir}\left(z_{\text{trop}}\right) - k\Delta U, \tag{21}$$

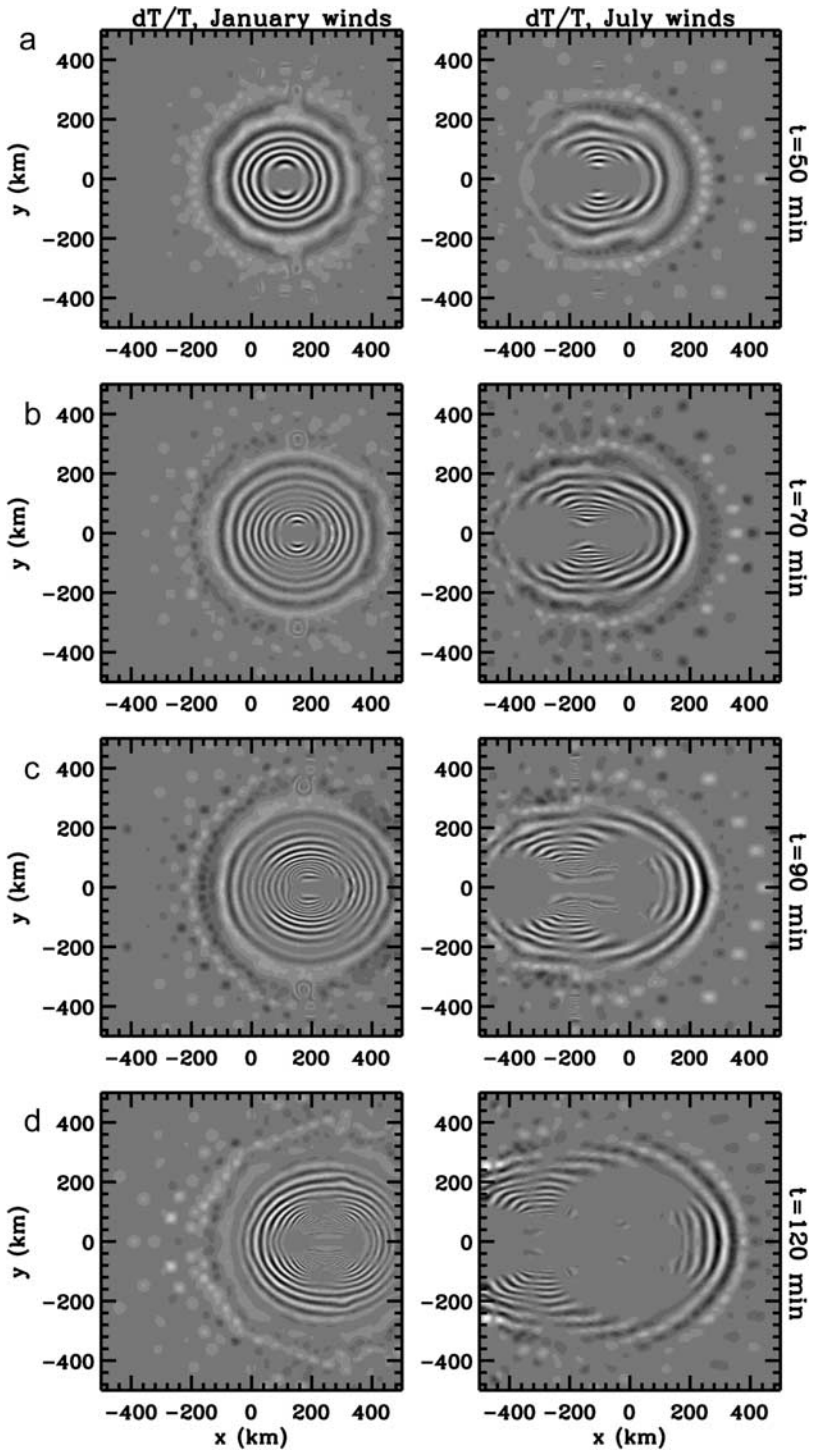

Figure 6. Same as in Figure 5, but for different winds. The results from the (left) January and (right) July zonal winds are shown. From left to right, the maximum value of $|T'/\overline{T}|$ are (a) 5.9 and 5.3%, (b) 4.9 and 3.4%, (c) 3.0 and 2.3%, and (d) 1.5 and 1.3%.

where $\Delta U = U(z) - U_{\text{trop}}$. Therefore for high-frequency, eastward propagating GWs with intrinsic frequencies at the tropopause ($\omega_{Ir}(z_{\text{trop}})$) close to N and having large k (i.e., small λ_x), since $\Delta U \sim -25$ m s^{-1} at $z = 87$ km and $-k\Delta U$ is positive, ω_{Ir} as calculated from equation (21) is larger than N at $z = 87$ km. Because GWs are not able to propagate with intrinsic frequencies larger than the buoyancy frequency, these waves become evanescent and reflect downward at lower altitude where $\omega_{Ir} \simeq N$ [*Cowling et al.*, 1971; *Waldock and Jones*, 1984]. From equation (3) and Figure 3, convectively generated GWs with small λ_x have small λ_z at the ridge of the spectrum. These GWs have small vertical

group velocities, since the vertical group velocity is approximately

$$c_{g,z} \sim -\frac{\omega_{Ir}}{m} \propto \lambda_z^2 \quad (22)$$

for GWs with $m^2 \gg k_H^2$ and $m^2 \gg 1/4H^2$, using equation (18). It therefore takes longer for these small λ_x and λ_z GWs to propagate to the OH airglow layer than the waves with large λ_x and λ_z. This is the reason the eastward moving portion of the GW spectrum is missing for $t \geq 90$ min, that these slowly propagating GWs with small λ_x and λ_z reflect below the OH layer where $\omega_{Ir}(z) = N$. At earlier times, the eastward propagating GWs have large λ_x and λ_z, thereby implying large vertical group velocities from equation (22). Because GWs with large λ_x have small k, most of these earlier GWs do not reflect in the stratosphere and mesosphere for this wind profile. On the other hand, those GWs propagating westward have $k < 0$; therefore, they do not reflect in this wind profile from equation (21), since $-k\Delta U$ is negative. Additionally, their intrinsic frequencies, vertical wavelengths, and vertical group velocities are smaller in the OH layer than those GWs propagating eastward. Since the maximum wave response at $z \sim 87$ km occurs at ~45–50 min after convective overshoot when the winds are zero, it is not surprising that the amplitudes of the westward propagating GWs are larger than those of the eastward propagating GWs at $t = 70$ min, since it takes these former waves more time than the latter waves to reach this altitude.

[33] Figure 7 shows the relative amplitudes of the GW temperature perturbations from Figure 5 for $y = 0$. One striking difference is that the highest-frequency GWs (those closest to the center of the convective plume) are present in the zero wind case for early times, but not in the April mean wind case. For the eastward propagating GWs, this occurs because of reflection (see equation (21)). For the westward propagating GWs, this occurs because these waves have horizontal wavelengths of $\lambda_x \sim 30$ km and $c_{IH} \sim 30$–40 m s^{-1} from Figure 3; therefore, they are removed by critical level filtering. For smaller frequencies or larger wave periods (which reach the mesopause at a radius of 100 km or greater from the plume center), the temperature amplitudes for the zero and April wind cases are similar at early times when the horizontal phase speeds are large. However, for $t \geq 70$ min, the amplitudes of the westward propagating GWs in the April winds are somewhat larger than for the zero wind case; this is because these former GWs arrive at $z = 87$ km later than if propagating through zero winds because their vertical group velocities are smaller. Because the overall amplitudes of the GWs decreases with time ~50 min after convective overshoot in the zero wind case, arriving later means that their amplitudes are larger than those in the zero wind case.

[34] We now discuss how variations in the winds at the launch altitude affect our results. The intrinsic phase speed, $c_{IH} = \omega_{Ir}/k_H$, can be expressed from equation (21) as

$$c_{IH}(z) = c_{IH}(z_{\text{trop}}) - \Delta U. \quad (23)$$

As mentioned previously, an eastward propagating GW reflects when the westward wind is too strong, causing the GW's intrinsic frequency to equal N. Using equation (23) and $c_{IH}(z) \geq N/k_H$, an rd propagating GW reflects from the wind if its initial intrinsic horizontal phase speed is larger than

$$c_{IH}(z_{\text{trop}}) \geq \lambda_H/\tau_b + \Delta U. \quad (24)$$

For GWs near the peak of the convective spectrum in Figure 3, $\lambda_H \sim 40$–60 km. Setting $\tau_b = 5.24$ min, then $\lambda_H/\tau_b \sim 130$–$190$ m s^{-1}. For the April wind case, $U(z_{\text{trop}}) \sim 30$ m s^{-1}; thus $\Delta U = -40$ m s^{-1} at $z \sim 80$ km. Therefore, those eastward propagating GWs near the peak of the spectrum will reflect off the westward wind if they have intrinsic phase speeds greater than $c_{IH}(z_{\text{trop}}) \geq 90$–$150$ m s^{-1}, using equation (24). But because the GW peak occurs with intrinsic phase speeds of $c_{IH}(z_{\text{trop}}) \sim 60$–$70$ m s^{-1} (see Figure 3), these peak eastward propagating GWs will therefore not reflect off this wind. (Note that these fast GWs can be observed at $t = 50$ min in Figure 5.) Now suppose the wind at z_{trop} is 10 m s^{-1} smaller. In this case, $\Delta U = -30$ m s^{-1} at $z \sim 80$ km, and these same peak GWs would reflect off the westward wind if they had intrinsic phase speeds greater than $c_{IH}(z_{\text{trop}}) \geq 100$–$160$ m s^{-1} instead. Because the GW spectrum peaks at smaller intrinsic phase speeds, these peak GWs would still not reflect downward from this smaller tropospheric wind.

[35] The situation is different for GWs with smaller horizontal wavelengths, however. For GWs with $\lambda_H \sim 20$–30 km, $\lambda_H/\tau_b \sim 60$–95 m s^{-1}. Therefore, those GWs with $c_{IH}(z_{\text{trop}}) \geq 20$–$55$ m s^{-1} for the April wind case reflect downward from the relative westward wind, using equation (24). Because nearly all of the GWs have intrinsic phase speeds larger than 30 m s^{-1} in Figure 3, most of the GWs with $\lambda_H \sim 20$ km reflect downward, while those GWs with $\lambda_H \sim 30$ km may or may not reflect, depending on their initial vertical wavelengths. However, if the wind at the tropopause is 10 m s^{-1} smaller, then these GWs would reflect downward from the westward wind if they have intrinsic phase speeds greater than $c_{IH}(z_{\text{trop}}) \geq 30$–$65$ m s^{-1}, which is less of a constraint. Therefore, if the wind at the tropopause is smaller, less of these smaller-scale GWs would reflect, leading to more eastward propagating GWs at later times at $z = 87$ km. Therefore, the smaller-scale, eastward propagating portion of the GW spectrum which is removed at later times depends sensitively on the wind at the tropopause.

[36] Because this April zonal wind profile is very similar to the wind profile deduced on 11 May 2004, as discussed earlier, we compare these model results with observations. For this weak wind profile, the model results show that the center of the CGWs is virtually the same as the center of the convective plume, within 20 km (see Figure 5). This matches the observations, which shows that the center of the CGWs is within 10 km of the center of the convective plume (within measurement accuracy) [*Yue et al.*, 2009]. Second, the model results show that the amplitudes of the eastward propagating GWs are significantly smaller than those of the westward propagating GWs for $t \geq 70$ min, and that for $t \geq 90$ min, no high-frequency, eastward propagating GWs with 40 km $< r <$ 200 km reach the mesopause. This result is caused by wave reflection, as discussed previously. Although the observation field of view (FOV) does not include a very large portion of the sky eastward of the center of the CGWs, the highest-frequency eastward

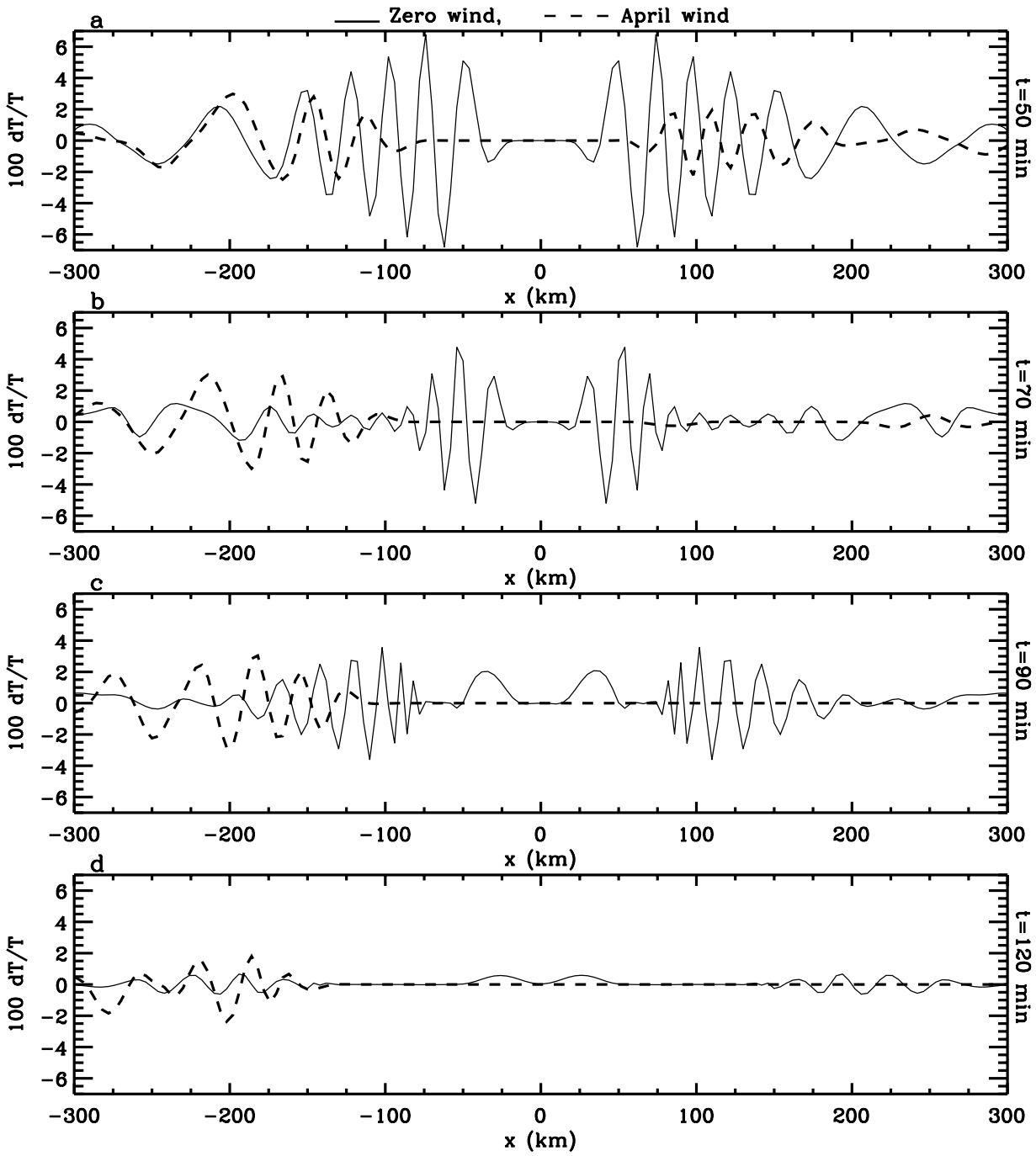

Figure 7. GW temperature perturbations $T'/\overline{T}$ (in %) at z = 87 km and y = 0 at (a) t = 50, (b) t = 70, (c) t = 90, and (d) t = 120 min. Solid lines show the zero wind results, and dashed lines show the April zonal wind results.

propagating GWs visible in the FOV can be seen from 0340 to 0410 UT, or 35 min < t < 65 min [see *Yue et al.*, 2009, Figure 1]. At later times, although westward propagating GWs are visible, eastward propagating GWs are not visible in the data. At the time, however, stars were visible in the eastern portion of the FOV; therefore, it is unlikely that clouds or poor seeing conditions were responsible for this deficit. Therefore, the lack of CGWs in the eastern portion of the FOV at late times may be due to wave reflection. Thus, the model results for the April wind case are qualitatively consistent with the OH imager observations.

[37] Next, consider the GWs ray-traced through the January mean zonal winds. Although the rings are 360°, the apparent center of the CGWs moves steadily eastward with time, reaching $x \sim 250$ km at t = 2 h. Additionally, at t = 70 min, λ_H is larger in the second white ring eastward of the apparent center (i.e., at $x \sim 240$ km) than in the second white ring westward of the apparent center (i.e., at

$x \sim -20$ km). Both of these aspects can be explained by Doppler shifting of the GWs in the mean background winds. First, the GWs are embedded in the mean winds at the tropopause of $\sim$30 m s^{-1}, and the winds continue to be eastward (and somewhat larger than this value) above this altitude up to $z \sim 80$ km. This causes all of the GWs to be swept downstream by an average advective velocity of $\sim$40 m s^{-1}, which is a horizontal distance of $\sim$300 km over 2 h. There is another way to think about this. Because the winds are eastward for $z < 80$ km, Doppler shifting causes the propagation paths of the eastward propagating GWs to be shallow, and those of the westward propagating GWs to be steep using equations (19) and (21); this causes the apparent center of the CGWs to shift eastward. Here, steeper (shallower) propagation paths correspond to smaller (larger) angle with the zenith and therefore a larger (smaller) intrinsic wave frequency from equation (19). This shift increases with time as the slower waves (with smaller frequencies and larger Doppler shifts) reach the mesopause. Note that the propagation paths from $z = 80$ to 87 km are not as important as those from $z = 12$ to 80 km, because the waves spend less time propagating through this smaller altitude range.

[38] Second, because the intervening winds are on average $\sim$40 m s^{-1} to the east, the vertical group velocities of eastward propagating GWs with zonal phase speeds greater than $\sim$50 m s^{-1} (in order to avoid critical level filtering) decrease in the mesosphere (below 80 km) because of decreasing vertical wavelengths from equations (21) and (22); at the same time, the vertical group velocities of westward propagating GWs increase in the mesosphere (below 80 km) [*Hines and Reddy*, 1967]. Although this trend reverses above 80 km, the net effect is that the westward propagating GWs arrive at the OH airglow layer before the eastward propagating GWs with the same λ_x. This causes eastward propagating GWs with large λ_x and large phase speeds to arrive at the OH layer at the same time as westward propagating GWs with smaller λ_x and smaller phase speeds. Note that those eastward propagating GWs with zonal phase speeds of $c_x < 50$ m s^{-1} (initial intrinsic zonal phase speeds of $c_{Ix} < 20$ m s^{-1}) meet critical levels and dissipate in the stratosphere or mesosphere at the altitude where $c_x \sim U$. Because our convective spectra has few of these GWs (see Figure 3), this effect does not eliminate very many eastward propagating GWs.

[39] Finally, consider the GWs ray traced through the July mean zonal winds. First, there is no single center for the CGWs. Since the meridional wind is assumed zero here, the "centers" are only displaced zonally; a realistic meridional wind would cause meridional displacements of the centers as well, and more arc-like and linear waves at $z \simeq 87$ km. Second, there are quite a few regions where no GWs are observed. This is due to (1) westward propagating GWs reaching critical levels in the stratosphere and mesosphere because of Doppler shifting via equation (21) such that $\omega_{Ir}(z) = 0$; (2) eastward propagating GWs reaching critical levels just below the mesopause from $z = 80$ to 87 km, and (3) high-frequency, eastward propagating GWs reflecting below $z < 80$ km at the altitude where $\omega_{Ir}(z) = N$.

[40] Although most of the eastward propagating GWs are missing for $t \geq 90$ min because of wave reflection, there are a few large-amplitude, eastward propagating CGWs at $x \sim 100-400$ km in the July wind case in Figure 6 that are very weak in the April wind case in Figure 5. The peak of these large-amplitude GWs moves eastward with time; it is located at $x \sim 280$ km at $t = 90$ min, and at $x \sim 360$ km at $t = 120$ min. It turns out that these eastward propagating GWs have small initial vertical wavelengths, are either upward or downward propagating initially from the convective plume, and have observed phase speeds of $c_H \sim 50$ m s^{-1}. Because the wind speed at the tropopause is $U_{\text{trop}} \sim 20$ m s^{-1}, their intrinsic horizontal phase speeds are $c_{IH} = c_H - U \sim 30$ m s^{-1}. These small-λ_z GWs appear in the lower portion of the convective spectrum in Figure 3, and have wavelengths of $\lambda_z \sim 10$ km and $\lambda_H \sim 60$ km. These GWs survive to $z = 80$ km in both the April and July winds because their initial vertical wavelength and frequencies are quite small. Therefore, although $-k\Delta U$ is large and positive in equation (21) (especially for the July wind case at $z \sim 70$ km), $\omega_{Ir}(z_{\text{trop}})$ is so small initially that $\omega_{Ir} < N$ at $z \sim 80$ km. However, because their amplitudes are only $\sim$30% of the amplitudes of those westward propagating GWs at the peak of the convective spectrum (i.e., at $\lambda_H \sim 50$ km and $\lambda_z \sim 25$ km), they do not have large $T'/\overline{T}$ amplitudes unless they are reaching critical levels, at which point $\omega_{Ir} \rightarrow 0$ and $T'/\overline{T}$ becomes large from equation (14).

[41] We choose a GW at this smaller peak of the convective spectrum as an example. If we ray trace an eastward propagating GW with $\lambda_H = 60$ km and $\lambda_z = 10$ km through the April wind model, it reaches $z = 87$ km at $t \sim 100$ min at $x \sim 300$ km. If we ray trace this same GW through the July winds, it reaches $z = 87$ km at a similar location and time: $t \sim 95$ min at $x \sim 220$ km. However, for the July wind model, this GW reaches a critical level at $z \sim 88-90$ km, since its observed phase speed is $c_x \sim 50$ m s^{-1} and the zonal wind is $U \sim 50$ m s^{-1} at $z \sim 90$ km from Figure 4d. Therefore, this GW has a very small intrinsic frequency at $z \sim 87$ km in the July wind model. From equation (14), this yields a large $T'/\overline{T}$ amplitude at $z = 87$ km, even though the vertical velocity amplitude is quite small (since the GW is propagating nearly horizontally) (see Figure 6). This same GW does not reach a critical level at this altitude in the April wind model; therefore, $T'/\overline{T}$ is small, and the GW is barely visible in Figure 5.

[42] In Figure 8, we show the vertical velocity perturbations for the same times as in Figures 5 and 6, but only for the April winds and the July winds. The vertical velocity perturbations look similar to the temperature perturbations for the April wind (see Figure 5). However, the vertical velocity perturbations are small at $x \sim 200-400$ km in the July winds, even though the temperature perturbations are large there (see Figure 6). This is because the temperature perturbation (but not the vertical velocity perturbation) becomes large as a GW approaches a critical level, as discussed above. Note that $\lambda_z \rightarrow 0$ as a GW approaches a critical level. Therefore, these GWs would likely not be easily visible in an OH airglow layer [*Swenson and Gardner*, 1998].

6. Comparison of Model Results With Data

[43] In this section, we compare our model results with the horizontal wavelengths and periods of the observed GWs. We also convert the observed intensity perturbations to tem-

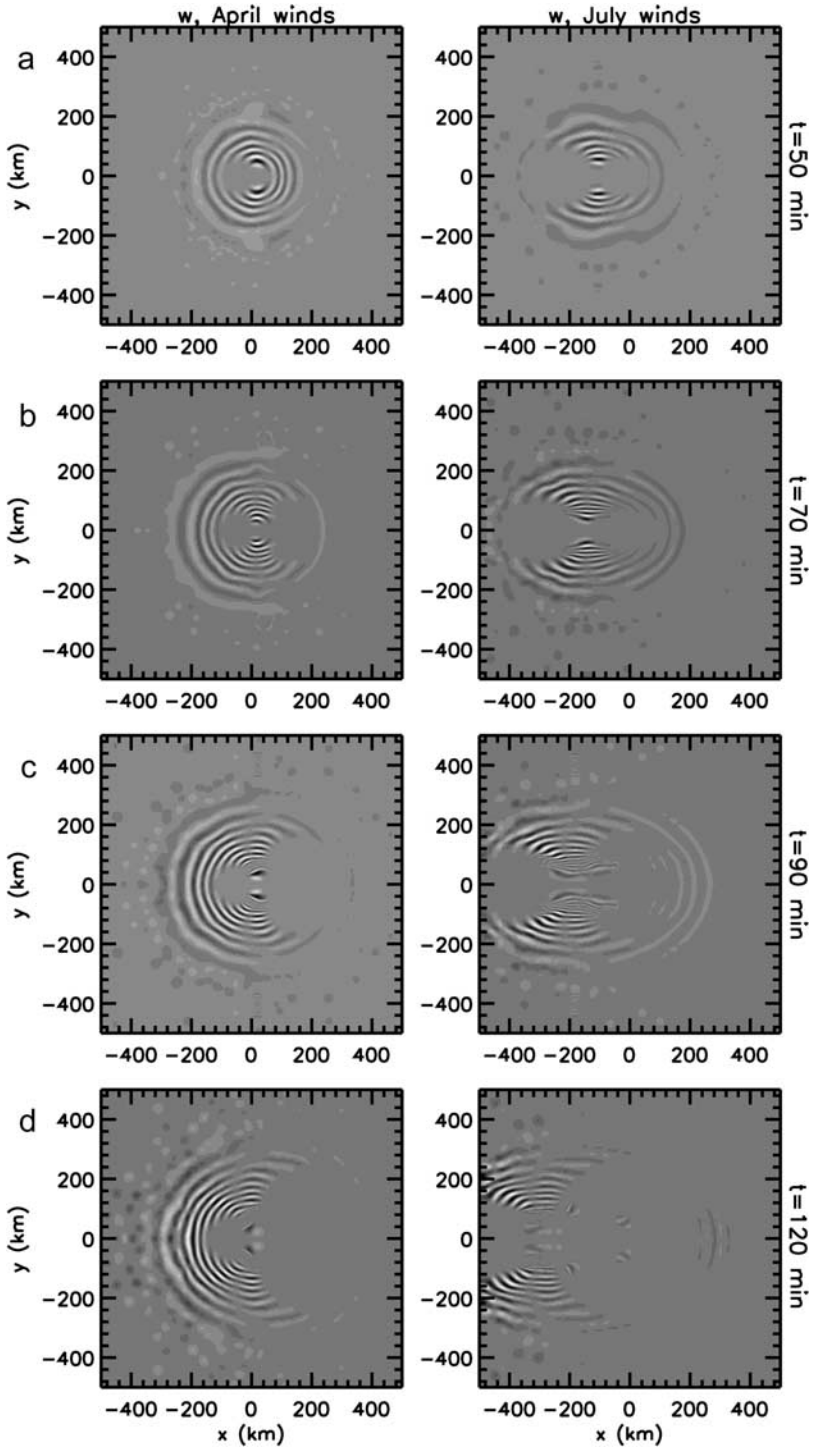

Figure 8. GW vertical velocity perturbations, w', at t = 50, 70, 90, and 120 min from the upper to lower rows, respectively. The results from the (left) April and (right) July zonal winds are shown. From left to right, the maximum values of $|w'|$ are (a) 26 and 22 m s^{-1}, (b) 17 and 13 m s^{-1}, (c) 9 and 7 m s^{-1}, and (d) 3.5 and 4 m s^{-1}.

perature perturbations, and compare our model results with observations for both the zero wind and April wind profiles.

6.1. Conversion of OH Intensities to GW Amplitudes

[44] We first describe how we convert the observed intensity perturbations to GW tem erature perturbations. One way to estimate the temperature perturbations from the intensity perturbations might be to use the Krassovsky parameter,

$$\eta \sim \left(I'/\overline{I}\right)/\left(T_I'/\overline{T_I}\right), \tag{25}$$

where T'_I is the intensity-weighted temperature perturbations. From *Schubert et al.* [1991] and *Swenson and Gardner*

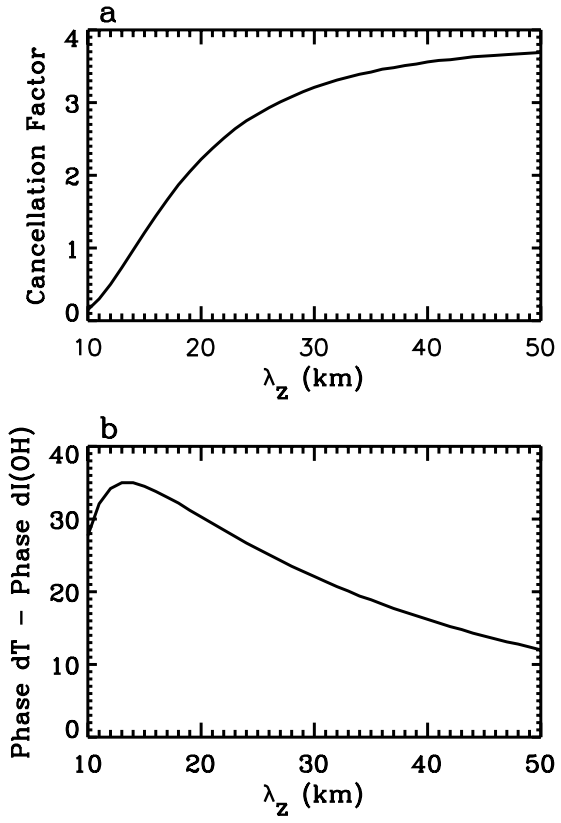

Figure 9. (a) Cancellation factor as a function of λ_z at z = 87 km. (b) Phase of $T'/\overline{T}$ at z = 87 km minus the phase of the intensity $I'/\overline{I}$ (OH), in degrees. Here, the wave is assumed saturated (β = 1) and has a period of 10 min. The background temperature profile is obtained from MSIS for 11 May 2004, and the background winds are assumed zero.

[1998], $\eta \sim 6$ and $\eta \sim 4-5$, respectively, for the wave scales and periods of the observed GWs (see section 6.2). However, T'_I is not the true GW temperature perturbation; it is the volume emission rate weighted temperature. Because the intensity perturbations in the OH airglow layer partially cancel out for $\lambda_z < 20-30$ km due to the finite thickness of the OH layer, it is important to utilize the intensity cancellation factor instead [*Swenson and Gardner*, 1998; *Liu and Swenson*, 2003]:

$$\mathrm{CF}_I = \frac{\max\left(I'/\overline{I}\right)}{\max\left(T'/\overline{T}\right)}. \tag{26}$$

Equation (26) relates the airglow intensity perturbation, $I'/\overline{I}$, to the GW temperature perturbation, $T'/\overline{T}$.

[45] Using a one-dimensional model which calculates the OH layer response for upward propagating GWs [*Liu and Swenson*, 2003], as well as the empirical NRLMSISE-00 model [*Hedin*, 1991], we calculate the cancellation factor for the OH airglow layer on 11 May 2004 for a GW with a 10 min wave period. Here, we have assumed that the wave is saturated (with a damping factor of β = 1), implying that the GW's amplitude is constant with altitude at $z \sim 90$ km [*Liu and Swenson*, 2003; *Vargas et al.*, 2007]. Note that this is generally a good appr tion for typical GWs observed by OH imagers [*Swenson et al.*, 2003]. We show the result in Figure 9a. We see that CF_I increases approximately linearly with λ_z from 0 to ~2.5 for λ_z = 10 to 20 km. For larger λ_z, CF_I increases more slowly, reaching a maximum value of $\mathrm{CF}_I \sim 3.7$ for $\lambda_z \rightarrow \infty$. This curve is similar to the result for a 2-h period GW (the dark dashed line in Figure 4 of *Liu and Swenson* [2003]).

[46] There is also a phase difference between T' and I'(OH). For concentric rings of propagating GWs in a zero wind, we can write the temperature perturbation T' at the altitude z as

$$T' = T'(0)\exp[i(k_H r - \omega_r t)], \tag{27}$$

where $T'(0)$ is the GW amplitude and r is the radius of the ring. This causes the intensity of the OH layer to oscillate in time and radius as

$$I'(\mathrm{OH}) = I'(\mathrm{OH})(0)\exp[i(k_H r - \omega_r t + \Delta\phi)]. \tag{28}$$

Here, $\Delta\phi$ is the phase of T' minus the phase of I'(OH), and I'(OH)(0) is the I' amplitude of the OH layer. Figure 9b shows the phase difference between T' at z = 87 km and I'(OH) for the same model as was used for Figure 9a. We see that the phase difference depends on λ_z, and is positive for all λ_z. This denotes that I' lags behind T' at z = 87 km in time at a fixed radius r. Or for a fixed time t, a peak in I' occurs at a smaller radius r than for T' at z = 87 km, from equations (27) and (28). Note that Figure 9b differs somewhat from the phase of the rotational temperature minus the phase of the OH intensity perturbations, because T'_R is different from T' (see the dashed line in Figure 6 of *Liu and Swenson* [2003]). We will use Figure 9 to convert the observed intensity perturbations $I'/\overline{I}$ (from Figure 1b) to the inferred temperature perturbations $T'/\overline{T}$ in section 6.2.

6.2. Comparison of Temperature Perturbations, Wavelengths, and Periods

[47] Because the April zonal wind profile from Figure 4d is likely representative of the winds on 11 May 2004, we compare the zero wind and the April wind results with the data here. In Figure 10, we show the model results at z = 87 km for zero winds (Figure 10, left), and for the April zonal winds (Figure 10, right). The model times are again measured from the time of convective overshoot. Figures 10a–10f show the average vertical wavelengths, average horizontal wavelengths, average wave periods, and temperature perturbations (in %). Here, the average horizontal wavelength, vertical wavelength, and wave period is calculated in each bin by weighing each GW's k_H, m, and ω_r, respectively, by its temperature perturbation amplitude. These model results are shown as a function of radii along a line 45° counterclockwise of north from the center of the plume. The model average vertical wavelengths in row 1 are shown at t = 55 min. We see that $\lambda_z \sim 15-50$ km for these GWs. The model horizontal wavelengths in row 2 increase with radius and decrease with time, as expected for freely propagating GWs excited from a convective plume [*Vadas and Fritts*, 2009]. Additionally, the model values of λ_H generally agree with the observations (shown as symbols at the corresponding times); however, the data values are somewhat larger than the model values for $r < 100$ km, and are somewhat smaller than the model values for $r > 200$ km.

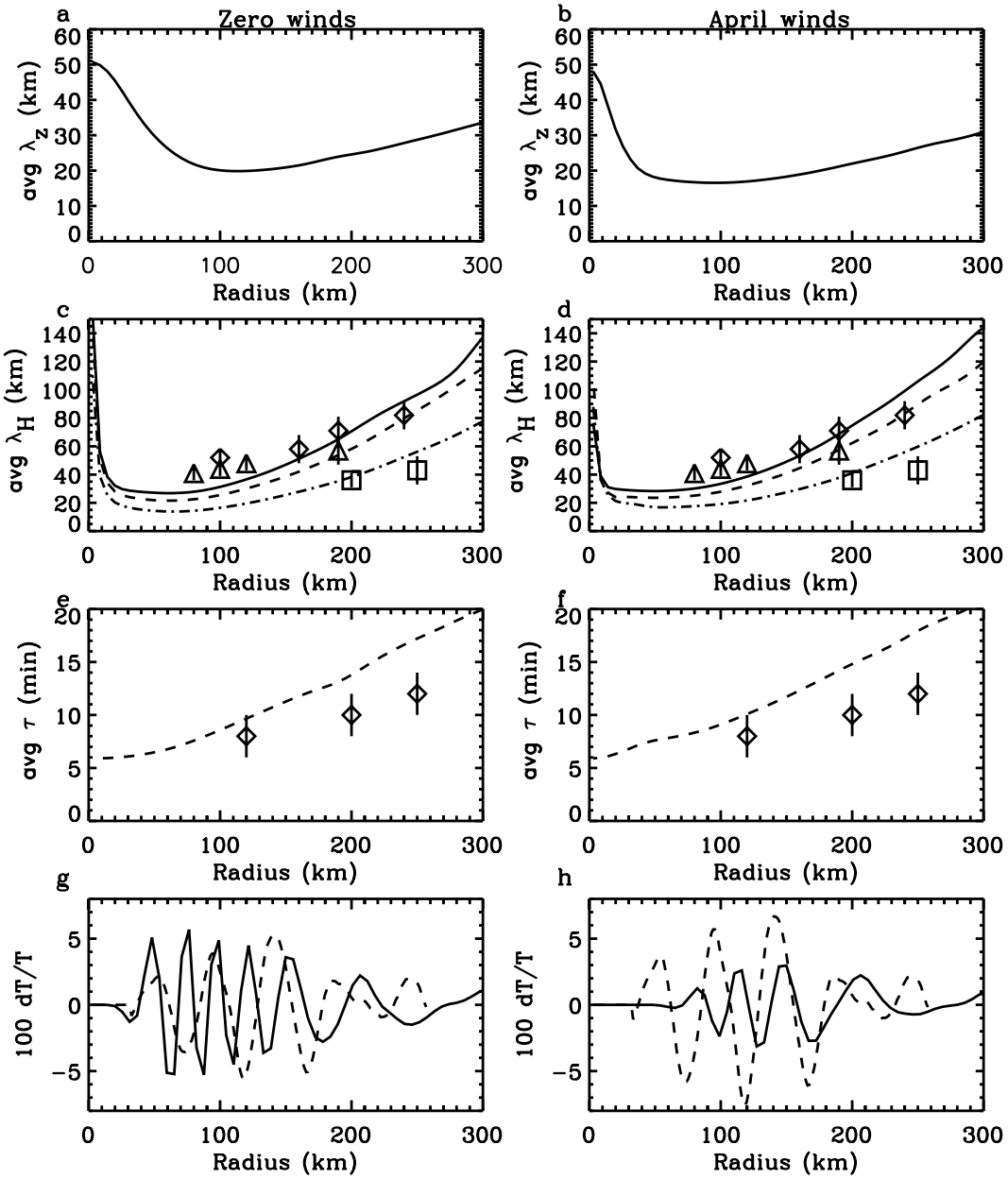

Figure 10. (left) Model results for zero winds. (right) Model results for the April zonal winds. (a, b) Model average vertical wavelengths at $t = 55$ min. (c, d) Model average horizontal wavelengths at $t = 45$, 55, and 85 min as solid, dashed, and dash-dotted lines, respectively. Data at 0350, 0400, and 0430 UT are shown as diamonds, triangles, and squares, respectively [*Yue et al.*, 2009]. (e, f) Model average ground-based wave periods at $t = 55$ min (dashed lines). Data at 0400 UT (diamonds). (g, h) Model temperature perturbations $T'/\overline{T}$ (in %) at $t = 55$ min along a line 45° to the northwest of the convective plume (solid lines). Inferred values of $T'/\overline{T}$ (from the data shown in Figure 1b) at 0400 UT (dashed lines).

Note that the model values of λ_H for $r < 20$ km are not accurate, because there are no GWs which enter these bins, thereby resulting in binned k_H values equal to zero there. In Figures 10e and 10f, we see that the model wave period at $r \sim 100$ km is similar to the data, whereas it is somewhat larger than the data for $r > 150$ km. Note that the wave periods from this convective plume model are somewhat improved over the wave periods obtained by *Yue et al.* [2009] using the windless Boussinesq GW dispersion relation.

[48] The model temperature perturbations $T'/\overline{T}$ (in %) in Figures 10g and 10h are shown at $t = 55$ min with solid lines. Because of critical level filtering from the winds [*Hines and Reddy*, 1967], there are fewer GWs at small radii for the April wind profile as compared to the zero wind case. Note that the data shows the presence of GWs at small radii, however. We also overlay the estimated temperature perturbations calculated from the observed intensity perturbations with dashed lines at the corresponding time of 0400 UT. Here, we first scale the intensity according to equation (26) in order to convert $I'/\overline{I}$ to $T'/\overline{T}$. Because the vertical wavelengths of

the observed waves are not known, we use the model values of λ_z in Figures 10a and 10b along with Figure 9a to determine CF_I as a function of radius. Then, we shift the intensity perturbations in radius via applying a phase shift of

$$r \rightarrow r + \Delta\phi/k, \tag{29}$$

using equations (27) and (28). Again, $\Delta\phi$ is determined from Figure 9b using the model values of λ_z from Figures 10a and 10b. Note that both CF_I and $\Delta\phi$ vary with radius, and are different for the zero and April wind cases because the model λ_z values are different (see Figures 10a and 10b). Therefore, the estimated values of $T'/\overline{T}$ as converted from the observed values of $I'/\overline{I}$ are different in Figures 10g and 10h for the zero and April wind cases. We see that the zero wind GW temperature perturbations are in reasonable agreement with the observed values, although the model perturbations are somewhat too large at small radii (large frequencies near N). Note also that the model temperature perturbation oscillates with a smaller λ_H than the observed values, as was noted previously for Figure 10c. For $r > 200$ km, the zero wind results agree reasonably well with the phase and amplitudes of the observed values. These larger radii waves have somewhat smaller frequencies, but have larger horizontal wavelengths, and thereby larger phase speeds. They are therefore less affected by the background winds. The model temperature perturbation amplitudes from the April zonal winds are ~2 times smaller than that inferred from observations for $r \sim 100-150$ km. For $r > 150$ km, however, the model $T'/\overline{T}$ results from the April winds are in better agreement with that inferred from the observations, because these larger-radii waves again have larger horizontal phase speeds. This agreement suggests that the parameters used in the convective plume model for convective plumes 1 and 2 on 11 May 2004, especially the updraft velocity and duration σ_t, are reasonable. It also suggests that the overall "envelope" approximation of the convective plume model yields good results at these larger λ_H wave scales.

[49] The April wind profile results in essentially no GWs for $r < 60$ km because of critical level filtering (solid line in Figure 10h), while the zero wind profile results in large-amplitude GWs at small radii (solid line in Figure 10g). The observations clearly show the presence of significant wave activity from $r = 30-60$ km, but with smaller amplitudes than for the zero wind profile. Because the observations show less critical level filtering than the April wind model results, but more critical level filtering than the zero wind model results, we conclude that the actual winds on 11 May were likely somewhat smaller than the April model zonal winds used here. One might argue that perhaps the winds were equal to zero at that time; after all, the rings in Figure 1a are near-perfect circles, and a slightly longer plume duration (σ_t) results in slightly smaller amplitudes for the highest-frequency GWs in the zero wind case, in better agreement with the observations. However, as mentioned in section 5, eastward propagating CGWs were not observed at later times (although the skies were clear and the westward propagating CGWs were visible); this was likely caused by reflection of eastward propagating GWs with small λ_H from increasing westward winds, as described in section 5. Therefore, it is unlikely that the winds were identicall equal to zero on 11 May 2004, although they were likely somewhat smaller than the April model winds used here.

7. Conclusions

[50] In this paper, we analyzed the role that wind filtering, Doppler effects, and mean flow advection play on the rings of concentric GWs (CGWs) excited from a modeled, vertically oriented convective plume on 11 May 2004 at 0305 UT near Fort Collins, Colorado. We used radar and satellite images to determine the typical plume parameters needed as inputs into a convective plume model. We then generated the excited GW spectrum from the convective overshoot of this plume into the stably stratified stratosphere. We ray traced these GWs from the tropopause through monthly (January, April, and July) zonal mean zonal winds derived from the HAMMONIA global scale model and lidar data. We found that the resulting temperature perturbations resembled circular concentric rings of GWs at $z = 87$ km only if the intervening winds were relatively constant with altitude. Additionally, large intervening winds caused the apparent center of the concentric rings to shift horizontally from the location of the convective plume. Arc-like patterns and "squashed" rings resulted when the winds were strong and variable with altitude. For GWs with $c_x < U$ propagating in the same direction as the winds, critical level filtering prevented some of the GWs from reaching $z = 87$ km. For GWs propagating in the opposite direction as the winds with $c_{IH}(z_{\text{trop}}) \geq \lambda_H/\tau_b + \Delta U$, evanescence and reflection when the wave's intrinsic frequency equaled the buoyancy frequency prevented some of the GWs from reaching $z = 87$ km.

[51] We then compared the zero and April wind results to OH airglow observations of CGWs. We found that the model horizontal wavelengths are in reasonable agreement with the data. However, the observed horizontal wavelengths for $r < 150$ km and $r > 200$ km were somewhat larger and smaller than the model values, respectively. Additionally, the model periods agreed well with observations at $r \sim 100-150$ km, although the observed wave periods were smaller than the model periods for $r > 150$ km. These differences may be due to the fact that we only modeled a single convective plume on 11 May 2004 at 0305 UT, while NEXRAD radar images showed that 2 deep convective plumes occurred nearly simultaneously at 0305 UT. Since these deep plumes were only separated by ~90 km, it is likely that the perturbation temperatures of the excited GWs created interference patterns in the airglow layers near the mesopause, creating somewhat different apparent wavelength and period profiles than that obtained via modeling a single plume. A more thorough study with several convective plumes and more realistic winds which include planetary wave and tidal variability are needed for better comparison with the observations.

[52] Finally, we compared the model temperature perturbations with the temperature perturbations inferred from the observed intensity perturbations using radially dependent cancellation factors and phase shifts. The model results generally agree well with the observations, demonstrating the reasonable accuracy of the convective plume model in describing the excited GW spectrum. However, there were some differences. In particular, we found that the April wind result showed too much critical level filtering at small radii where the frequencies are large. We also found that the zero

wind result showed not enough critical level filtering at small radii, as compared to observations. We concluded that the actual winds on 11 May were likely somewhat smaller than the April zonal winds used here, although they were unlikely equal to zero. This is because eastward propagating GWs were not observed at late times near the center of the CGWs, as predicted by the April wind model result. This deficit is caused by evanescence and reflection of high-frequency, eastward propagating GWs from an increasing westward wind with altitude.

[53] **Acknowledgments.** The authors would like to thank Hauke Schmidt for the HAMMONIA model data. S.L.V. would like to thank James Hecht for useful discussions. This research was supported by NSF grant ATM-0537311 (at NWRA), by NASA NNX07AB64G and NSF ATM-0545221 (at CSU), and by NSF grant ATM 0737656 (at UI).

References

Alexander, M. J., J. R. Holton, and D. R. Durran (1995), The gravity wave response above deep convection in a squall line simulation, *J. Atmos. Sci.*, *52*, 2212–2226.

Beres, J. H. (2004), Gravity wave generation by a three-dimensional thermal forcing, *J. Atmos. Sci.*, *61*, 1805–1815.

Bluestein, H. B., E. W. McCaul Jr., G. P. Byrd, and G. R. Woodall (1988), Mobile sounding observations of a tornadic storm near the dryline: The Canadian, texas storm of 7 May 1986, *Mon. Weather Rev.*, *116*, 1790–1804.

Cowling, D. H., H. D. Webb, and K. C. Yeh (1971), Group rays of internal gravity waves in a wind-stratified atmosphere, *J. Geophys. Res.*, *76*, 213–220.

Dewan, E. M., R. H. Picard, R. R. ONeil, H. A. Gardiner, J. Gibson, J. D. Mill, E. Richards, M. Kendra, and W. O. Gallery (1998), MSX satellite observations of thunderstorm-generated gravity waves in mid-wave infrared images of the upper stratosphere, *Geophys. Res. Lett.*, *25*, 939–942.

Fovell, R. D. Durran, and J. R. Holton (1992), Numerical simulations of convectively generated stratospheric gravity waves, *J. Atmos. Sci.*, *49*, 1427–1442.

Gossard, E. E., and W. H. Hooke (1975), *Waves in the Atmosphere*, 456 pp., Elsevier Sci., Amsterdam.

Hedin, A. E. (1991), Extension of the MSIS thermosphere model into the middle and lower atmosphere, *J. Geophys. Res.*, *96*, 1159–1172.

Hines, C. O. (1960), Internal atmospheric gravity waves at ionospheric heights, *Can. J. Phys.*, *38*, 1441–1481.

Hines, C. O. (1967), On the nature of travelling ionospheric disturbances launched by low-altitude nuclear explosions, *J. Geophys. Res.*, *72*, 1877–1882.

Hines, C. O., and C. A. Reddy (1967), On the propagation of atmospheric gravity waves through regions of wind shear, *J. Geophys. Res.*, *72*, 1015–1034.

Holton, J. R., and M. J. Alexander (1999), Gravity waves in the mesosphere generated by tropospheric convention, *Tellus, Ser. B*, *51*, 45–58, doi:10.1034/j.1600-0889.1999.00005.x.

Horinouchi, T., T. Nakamura, and J. Kosaka (2002), Convectively generated mesoscale gravity waves simulated throughout the middle atmosphere, *Geophys. Res. Lett.*, *29*(21), 2007, doi:10.1029/2002GL016069.

Lane, T. P., M. J. Reeder, and T. L. Clark (2001), Numerical modeling of gravity waves generated by deep tropical convection, *J. Atmos. Sci.*, *58*, 1249–1274, doi:10.1175/1520-0469(2001)058<1249:NMOGWG>2.0.CO;2.

Lane, T. P., R. D. Sharman, T. L. Clark, and H.-M. Hsu (2003), An Investigation of turbulence generation mechanisms above deep convection, *J. Atmos. Sci.*, *60*, 1297–1321.

Larsen, M. F., W. E. Swartz, and R. F. Woodman (1982), Gravity-wave generation by thunderstorms observed with a vertically-pointing 430 MHz radar, *Geophys. Res. Lett.*, *9*, 571–574.

Lighthill, J. (1978), *Waves in Fluids*, Cambridge Univ. Press, Cambridge, U.K.

Liu, A. Z., and G. R. Swenson (2003), A modeling study of O_2 and OH airglow perturbations induced by atmospheric gravity waves, *J. Geophys. Res.*, *108*(D4), 4151, doi:10.1029/2002JD002474.

Piani, C., D. Durran, M. J. Alexander, and J. R. Holton (2000), A numerical study of three dimensional gravity waves triggered by deep tropical convection, *J. Atmos. Sci.*, *57*, 3689–3702.

Renick, J. H., and J. B. Maxwell (1977), Forecasting hailfall in Alberta, *Meteorol. Monogr.*, *38*, 145–151.

Roble, R. G., and E. C. Ridley (1994), A thermosphere-ionosphere-mesosphere-electrodynamics general circulation model (TIME-GCM): Equinox solar cycle minimum simulations (30–500 km), *Geophys. Res. Lett.*, *21*, 417–420.

Schmidt, H., G. P. Brasseur, M. Charron, E. Manzini, M. A. Giorgetta, T. Diehl, V. I. Fomichev, D. Kinnison, D. Marsh, and S. Walters (2006), The HAMMONIA chemistry climate model: Sensitivity of the mesopause region to the 11-year solar cycle and CO_2 doubling, *J. Clim.*, *19*, 3903–3931.

Schubert, G., R. L. Walterscheid, and M. P. Hickey (1991), Gravity wave-driven fluctuations in OH nightglow from an extended, dissipative emission region, *J. Geophys. Res.*, *96*, 13,869–13,880.

Sentman, D. D., E. M. Wescott, R. H. Picard, J. R. Winick, H. C. Stenbaek-Nielsen, E. M. Dewan, D. R. Moudry, F. T. Sao Sabbas, M. J. Heavner, and J. Morrill (2003), Simultaneous observations of mesospheric gravity waves and sprites generated by a midwestern thunderstorm, *J. Atmos. Sol. Terr. Phys.*, *65*, 537–550, doi:10.1016/S1364-6826(02)00328-0.

She, C.-Y., and R. P. Lowe (1998), Seasonal temperature variations in the mesopause region at mid-latitude: comparison of lidar and hydroxyl rotational temperatures using WINDIIUARS OH height profiles, *J. Atmos. Terr. Phys.*, *60*, 1573–1583.

Suzuki, S., K. Shiokawa, Y. Otsuka, T. Ogawa, K. Nakamura, and T. Nakamura (2007), A concentric gravity wave structure in the mesospheric airglow images, *J. Geophys. Res.*, *112*, D02102, doi:10.1029/2005JD006558.

Swenson, G. R., and C. S. Gardner (1998), Analytical models for the responses of the mesospheric OH* and Na layers to atmospheric gravity waves, *J. Geophys. Res.*, *103*, 6271–6294.

Swenson, G. R., and S. B. Mende (1994), OH emissions and gravity waves (including a breaking wave) in all-sky imagery from Bear Lake, *Utah, Geophys. Res. Lett.*, *21*, 2239–2242.

Swenson, G. R., A. Z. Liu, and J. Tang (2003), High frequency atmospheric gravity wave damping in the mesosphere, *Adv. Space Res.*, *32*, 785–793.

Taylor, M. J., and M. A. Hapgood (1988), Identification of a thunderstorm as a source of short period gravity waves in the upper atmospheric nightglow emissions, *Planet. Space Sci.*, *36*, 975–985.

Taylor, M. J., M. B. Bishop, and V. Taylor (1995), All-sky measurements of short period waves imaged in the OI (557.7 nm), Na (589.2 nm) and near infared OH and O2 (0,1) nightglow emissions during the ALOHA-93 campaign, *Geophys. Res. Lett.*, *22*, 2833–2836.

Vadas, S. L. (2007), Horizontal and vertical propagation and dissipation of gravity waves in the thermosphere from lower atmospheric and thermospheric sources, *J. Geophys. Res.*, *112*, A06305, doi:10.1029/2006JA011845.

Vadas, S. L., and D. C. Fritts (2001), Gravity wave radiation and mean responses to local body forces in the atmosphere, *J. Atmos. Sci.*, *58*, 2249–2279.

Vadas, S. L., and D. C. Fritts (2004), Thermospheric responses to gravity waves arising from mesoscale convective complexes, *J. Atmos. Sol. Terr. Phys.*, *66*, 781–804.

Vadas, S. L., and D. C. Fritts (2005), Thermospheric responses to gravity waves: Influences of increasing viscosity and thermal diffusivity, *J. Geophys. Res.*, *110*, D15103, doi:10.1029/2004JD005574.

Vadas, S. L., and D. C. Fritts (2009), Reconstruction of the gravity wave field excited by convective plumes via ray tracing in real space, *Ann. Geophys.*, *27*, 147–177.

Vargas, F., G. Swenson, A. Liu, and D. Gobbi (2007), $O(^1S)$, OH, and O_2 (b) airglow layer perturbations due to AGWs and their implied effects on the atmosphere, *J. Geophys. Res.*, *112*, D14102, doi:10.1029/2006JD007642.

Waldock, J. A., and T. B. Jones (1984), The effects of neutral winds on the propagation of medium-scale atmospheric gravity waves at mid-latitudes, *J. Atmos. Terr. Phys.*, *46*, 217–231.

Walterscheid, R. L., G. Schubert, and D. G. Brinkman (2001), Small-scale gravity waves in the upper mesosphere and lower thermosphere generated by deep tropical convection, *J. Geophys. Res.*, *106*, 31,825–31,832.

Yuan, T., C.-Y. She, D. A. Krueger, F. Sassi, R. Garcia, R. G. Roble, H.-L. Liu, and H. Schmidt (2008), Climatology of mesopause region temperature, zonal wind, and meridional wind over Fort Collins, Colorado (41°N, 105°W), and comparison with model simulations, *J. Geophys. Res.*, *113*, D03105, doi:10.1029/2007JD008697.

Yue, J., S. L. Vadas, C.-Y. She, T. Nakamura, S. C. Reising, H.-L. Liu, P. A. Stamus, D. A. Krueger, W. Lyons, and T. Li (2009), Concentric gravity waves in the mesosphere generated by deep convective plumes in the lower atmosphere near Fort Collins, Colorado, *J. Geophys. Res.*, *114*, D06104, doi:10.1029/2008JD011244.

A. Z. Liu, Department of Electrical and Computer Engineering, University of Illinois at Urbana-Champaign, 1308 West Main Street, 308 CSL, Urbana, IL 61801-0000, USA.

C.-Y. She and J. Yue, Department of Physics 1875, Colorado State University, Fort Collins, CO 80523-0000, USA.

P. A. Stamus and S. L. Vadas, CoRA Division, NWRA, 3380 Mitchell Lane, Boulder, CO 80301, USA. (vasha@cora.nwra.com)